# Ab initio prediction of the rovibrational levels of the He-CO+ ionic complex

M. Mladenovic, Marius Lewerenz

*Molecular Physics*
Vol. 00, No. 00, Month 2013, 1–28

## RESEARCH ARTICLE

# Ab initio prediction of the rovibrational levels of the He-$CO^+$ ionic complex

Mirjana Mladenović[a]* and Marius Lewerenz[a]

[a] *Université Paris-Est, Laboratoire Modélisation et Simulation Multi Echelle, MSME UMR 8208 CNRS, 5 bd Descartes, 77454 Marne la Vallée, France*

(*January 2013*)

The intermolecular potential for the van der Waals complex of the carbon monoxide cation with helium is studied by means of the partially spin adapted coupled cluster RCCSD(T) method and the aug-cc-pVXZ family of basis sets. In the ground electronic state, correlated with the lowest electronic asymptote $X^2\Sigma^+$ of the monomer $CO^+$, the complex He($^1S$)-$CO^+$($^2\Sigma^+$) has a nonlinear equilibrium structure with a Jacobi angle of about 46° and a binding energy of about 275 cm$^{-1}$. For the complex He($^1S$)-$CO^+$($A^2\Pi$) we find equilibrium Jacobi angles of 78° and 90° and electronic binding energies of about 160 cm$^{-1}$ and 303 cm$^{-1}$ for the $A''$ and $A'$ components, respectively, coalescing into the $\Pi$ state at linearity. Two-dimensional intermolecular potential energy surfaces are constructed for the ground electronic state and used to compute rotation-vibration states up to $J = 10$ with the numerically exact discrete variable representation (DVR) technique. The He-$CO^+$ complex is found to have 19 bound even-parity $J = 0$ states and 16 bound odd-parity $J = 1$ states and to exhibit strong angular-radial coupling and quasilinear behaviour.

**Keywords:** molecular ions; van der Waals complex; carbon monoxide cation; helium; rovibrational structure; ab initio calculation; electric properties; quadrupole moment

## 1. Introduction

Carbon monoxide is a relatively abundant molecule in interstellar space, where its positive ion $CO^+$ has also been identified [1, 2]. Even before its laboratory observation the $A^2\Pi - X^2\Sigma^+$ system in $CO^+$ was observed in the tail of a comet [3, 4] and is still known as 'comet-tail bands'. $CO^+$ was the first molecular ion for which a microwave spectrum was recorded [5]. Low energy collisions of $CO^+$ with its second most abundant collision partner in space, helium atoms, are governed by the weak intermolecular interaction leading to the van der Waals complex He-$CO^+$. Evidence for the formation of this complex has been observed in several ion drift tube experiments: conventional measurements at room temperature [6], laser-induced fluorescence measurements from various initial rotational states at 305 K [7], and ion drift tube measurements at very low temperatures [8]. No high resolution spectral data have ever been reported for this complex.

The relatively strong binding between $CO^+$ and helium atoms should allow the creation of mixed clusters of the composition He$_n$-$CO^+$ in drift tubes or mixed gas expansions coupled to electric discharges. The latter technique has been successfully applied in a series of elegant spectroscopic experiments on the energetically very

*Corresponding author. Email: mladenov@univ-mlv.fr

ISSN: 0026Ű8976 print/ISSN 1362Ű3028 online

DOI: 10.1080/0026897YYxxxxxxxx

similar $He_n$-$N_2^+$ complexes [9–12], where size selected high resolution spectra could be recorded. High resolution infrared spectroscopy of Ar-$N_2^+$ created in a plasma slit jet experiment has been recently reported [13] indicating the possibility of an infrared experiment on He-$CO^+$.

$He_n$-$CO^+$ clusters appear to be an ideal target for cluster size specific high resolution depletion spectroscopy. Both microwave and infrared experiments would profit from the large permanenent dipole moment and large vibrational transition moments of this system. Experiments on this type of cluster would help us to better understand microscopic superfluidity [14] by explicit control of the system size and measurement of the cluster size dependent evolution of the effective rotational constant of the $CO^+$ dopant. Neutral CO molecules embedded into large helium clusters have been studied theoretically [15–18] and experimentally by high resolution spectroscopy [17, 19–23]. Recent ionization experiments on CO doped large helium clusters did not yield any indication for the formation of $He_n$-$CO^+$ fragments whereas species of the type $He_n$-$(CO)_m^+$ were readily observed [24]. The $CO/CO^+$ pair inside helium is of particular interest for high resolution experiments because the rotational constants of both species are very similar while their interaction with helium atoms is of very different strength. Theoretical and experimental studies of $He_n$-$CO^+$ can make a major contribution to this field.

The He-$CO^+$ complex has been only partially characterized in earlier theoretical studies [24–28]. Hamilton *et al.* [25] employed unrestricted Hartree-Fock and Møller-Plesset perturbation theory to fourth order (MP4) to study linear and T-shaped arrangements for the ground and first excited electronic states. For linear and T-shaped He-$CO^+$ in the ground electronic state, Lotrich and van der Avoird [27] tested a new method for the determination of interaction energies of cationic complexes from interaction energies and vertical ionization potentials of neutral species. Salazar *et al.* [28] used spin unrestricted open-shell coupled cluster theories in combination with the cc-pVTZ basis set plus bond functions and identified bent equilibrium geometries with a Jacobi angle of $\theta_e = 45°$, a Jacobi distance of $R_e = 2.85$ A and a binding energy of $D_e = 275$ cm$^{-1}$ for the ground electronic state, whereas they found $\theta_e = 90^\circ$, $R_e = 2.70$ A and $D_e = 218$ cm$^{-1}$ for the first excited electronic state. A MP4 potential energy surface developed by Maclagan *et al.* [26] was used in classical trajectory calculations for the transport cross sections of $CO^+$ ions in helium gas.

The main purpose of the present study of He-$CO^+$ is the construction of an accurate potential energy surface and the prediction and interpretation of accurate vibration-rotation levels which could be checked against future detailed spectroscopic experiments. This potential surface will serve as a building block in many-body models for $CO^+$ ions inside larger helium clusters [29].

*Ab initio* calculations have been carried out with supermolecule coupled cluster techniques in combination with the aug-cc-pVXZ family of basis functions for the ground and first excited electronic states. The counterpoise procedure of Boys and Bernardi and extrapolations to infinite basis size have been used to correct for finite basis size effects on the shape of the surface and in particular on the dissociation energy and the equilibrium geometry (Section 2). In addition to the structural parameters, we have also studied the spectroscopic and electric properties of the monomers (Section 3) and the complex (Section 4) in the ground and first excited electronic states. The complex He-$CO^+$ is bound by induction and dispersion forces, responsible for long-range attraction between the two monomers. Two-dimensional (2D) intermolecular potential energy surfaces have been constructed for He-$CO^+$ in the ground electronic state (Section 5) and are used to calculate the rovibrational energy spectra by a numerically exact method based on a discrete variable repre-

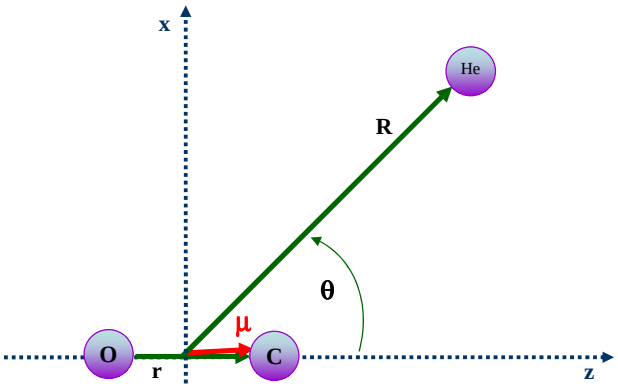


Figure 1. Jacobi coordinates $r, R, \theta$ and the axis system used for the van der Waals complex He-$CO^+$. The dipole moment vector $\boldsymbol{\mu}$ corresponding to the equilibrium structure of the complex is also shown.

sentation (Section 6). The complex is found to belong to the class of quasi-linear molecules. Indications for low energy resonances are also observed.

## 2. Electronic structure calculations

The *ab initio* computations have been carried out by means of the partially spin adapted coupled-cluster RCCSD(T) method with full iterative treatment of single and double excitations and perturbative correction for triple substitutions [30**?** , 31], as implemented in the MOLPRO quantum chemistry program package [32]. The singly augmented correlation consistent polarized valence basis sets, commonly labelled aug-cc-pVXZ, have been used [33, 34]. Fully relaxed geometry optimizations and harmonic frequency determinations were performed by means of numerical derivatives.

The three Jacobi coordinates $r$, $R$, and $\theta$, shown in Figure 1, are employed to describe the internal geometry of the complex. Here, $r$ is the bond length of the diatomic fragment $CO^+$, $\mathbf{R}$ is a vector of length $R$ running from the center-of-mass of the diatom to the He atom, and $\theta$ is the angle enclosed by $\mathbf{R}$ and the $CO^+$ axis. The Jacobi angle $\theta$ is measured from the C side of $CO^+$, such that $\theta = 0°$ corresponds to a linear complex with He closer to carbon.

The interaction energies of the complex were calculated in the supermolecular approach as

$$E_{int} = E_{ab}(AB) - E_a(A) - E_b(B), \tag{1}$$

where AB, A, and B stand respectively for He-$CO^+$, He, and $CO^+$. The lower index $p$ in $E_p(Q)$ refers to the basis set of the species $P$ used to compute the energy $E(Q)$ for the species $Q$. The interaction energies $E_{int}$ were corrected for the basis set superposition error (BSSE) by means of the counterpoise correction (CP) method of Boys and Bernardi [35], giving the CP corrected interaction energy $E_{int}^{\mathrm{CP}}$ as

$$E_{int}^{\mathrm{CP}} = E_{ab}(AB) - E_{ab}(A) - E_{ab}(B), \tag{2}$$

where the monomer and complex wavefunctions are all computed in the basis set of the complex. The geometry optimizations were carried out at the CP uncorrected level.

The interaction energies at the complete basis set (CBS) limit were estimated by means of the two-step procedure of Helgaker *et al.* [36] which employs an exponential

extrapolation for the Hartree-Fock Self-Consistent Field (SCF) contribution

$$E^{\mathrm{SCF}}(X) = E^{\mathrm{SCF}}_{\infty} + ae^{-bX} \tag{3}$$

and a $1/X^3$ extrapolation for the correlation part

$$E^{\mathrm{corr}}(X) = E^{\mathrm{corr}}_{\infty} + c/X^3, \tag{4}$$

where $X$ denotes the basis set cardinal number. In this fashion, the estimated total CBS energy for species Q becomes

$$E_{\infty}(Q) = E^{\mathrm{SCF}}_{\infty}(Q) + E^{\mathrm{corr}}_{\infty}(Q) \tag{5}$$

and the interaction energy is computed from the best total energy estimates as

$$E_{int} = E_{\infty}(\mathrm{He} - \mathrm{CO}^+) - E_{\infty}(\mathrm{He}) - E_{\infty}(\mathrm{CO}^+). \tag{6}$$

The electric dipole moments $\mu_q$ and electric quadrupole moments $\Theta_{ij}$ with $i, j = x, y, z$ were obtained numerically at the RCCSD(T) level of theory by means of finite-field calculations, using field strengths of 0.001-0.00005 a.u. It is noted that $\Theta_{xx} + \Theta_{yy} = -\Theta_{zz}$ holds for the quadrupole moment $\Theta$, which is a traceless second moment tensor. The electric properties reported in the present work were evaluated with respect to the axis system $x, y, z$ shown in Figure 1, where the $z$-axis is along the diatom bond vector $\mathbf{r}$, the $z \wedge x$ plane coincides with the molecular plane, and the origin of the frame is at the center of mass of the $^{12}C^{16}O^+$ unit.

The quality of our RCCSD(T) calculations was investigated by means of several other electronic-structure approaches, including the complete active space self-consistent field method (CASSCF), multi-reference Rayleigh-Schrödinger second-order perturbation theory (RS2) in connection with the multi-state multi-reference complete active space perturbation theory (CASPT2), and the multi-reference internally contracted configuration interaction (MRCI) method [37–39]. The latter approaches were particularly useful for the calculation of geometric and electric properties of the electronic state $2^2A'$ of the complex He-$CO^+$.

## 3. Monomer properties

### 3.1. *Carbon monoxide cation*

The ground state electronic configuration of CO is $(1\sigma)^2(2\sigma)^2(3\sigma)^2(4\sigma)^2(1\pi)^4(5\sigma)^2$. Removal of an electron from the highest energy $\sigma$ orbital leads to the ground electronic state $(1\sigma)^2(2\sigma)^2(3\sigma)^2(4\sigma)^2(1\pi)^4(5\sigma)^1$ of $CO^+$ which is $X^2\Sigma^+$. Removal of an electron from the $1\pi$ orbital leads to $A^2\Pi_i$ as the first excited state, $(1\sigma)^2(2\sigma)^2(3\sigma)^2(4\sigma)^2(1\pi)^3(5\sigma)^2$, which is split by a spin-orbit interaction constant $A_{SO}$ of -117.5 cm$^{-1}$ (Ref. [40]). The singly occupied $5\sigma$ molecular orbital of $CO^+(X^2\Sigma^+)$ is primarily composed of the $2s, 2p_z$ atomic orbitals of C, whereas the singly occupied $1\pi$ molecular orbital of $CO^+(A^2\Pi)$ is primarily composed of the out-of-bond-line $2p_{x,y}$ atomic orbital of oxygen.

Atomic oxygen has a $^3P_g$ ground state which is split by spin-orbit interaction into $^3P_2$ at $E = 0$, $^3P_1$ at $E = 158.265$ cm$^{-1}$, $^3P_0$ at $E = 226.977$ cm$^{-1}$, and has an ionization limit of 150305.6 cm$^{-1}$ leading to $O^+(^4S_u)$. The carbon atom ground state $^3P_g$ asymptote is split into $^3P_0$ at $E = 0$, $^3P_1$ at $E = 16.40$ cm$^{-1}$, $^3P_2$ at $E = 43.40$ cm$^{-1}$. The carbon atom ionization limit is 90820.42 cm$^{-1}$ leading to

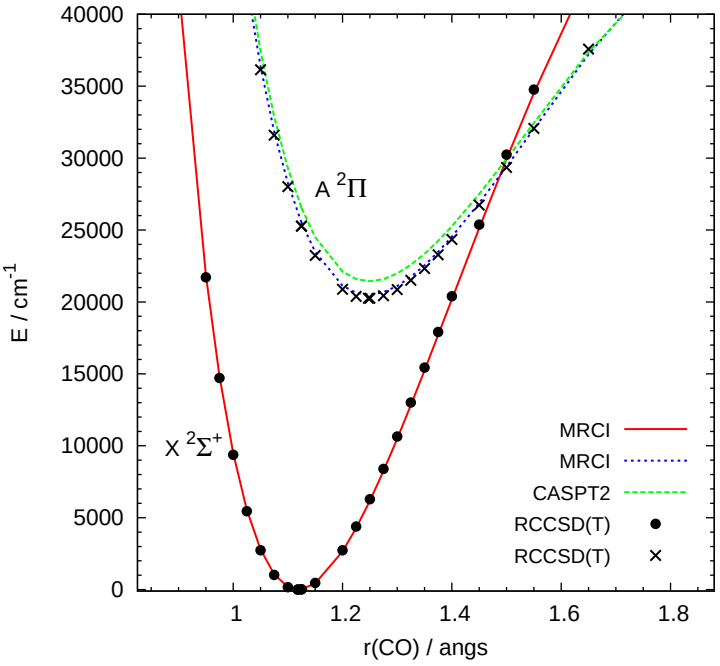


Figure 2. Potential energy curves for the $X^2\Sigma^+$ and $A^2\Pi$ states of $CO^+$ from the RCCSD(T), three-state CASPT2, and MRCI calculations with the aug-cc-pVQZ basis set.

$C^+(^2P_{1/2})$ and to $C^+(^2P_{3/2})$ at 90883.84 $cm^{-1}$. The lowest dissociation asymptote for $CO^+$ is therefore $C^+(^2P_u)$ + $O(^3P_g)$ which correlates with the molecular states $^{(2,4)}(\Sigma^+, \Sigma^-, \Sigma^-, \Pi, \Pi, \Delta)$.

The $^2\Sigma^+$ and $^2\Pi$ curves of $CO^+$ cross at about $r = 1.5$ Å at an energy approximately 30000 $cm^{-1}$ above the potential energy minimum of the ground electronic state, as found in our CASPT2 and MRCI calculations with the basis set aug-cc-pVQZ (see Figure 2). This finding is in agreement with Rydberg-Klein-Rees curves derived by Coxon and Foster [41] in their deperturbation analysis of the $A^2\Pi \leftrightarrow X^2\Sigma^+$ spectroscopic data. The $\Omega = 1/2$ components of these two states are mixed by spin-orbit coupling which affects accidentally near-degenerate zero-order vibration-rotation levels in the two electronic states at energies far below the electronic intersection energy. This is the origin of the perturbations observed [41–43] in the $A^2\Pi(v = 0)$ state by rotational levels of the $X^2\Sigma^+(v = 10)$ state, both lying about 22000 $cm^{-1}$ above the minimum (Figure 1 of Ref. [41]).

In the present work, we consider the electronic states $X^2\Sigma^+$ and $A^2\Pi$ of $CO^+$ within the Born-Oppenheimer approximation, aiming only at a good zero-order (adiabatic) description. Spin-orbit interaction and its effect on rovibrational spectra of $CO^+$ will be an important part of a future study.

### *3.1.1. Results for $CO^+$*

Structural, spectroscopic, and electric properties of the carbon monoxide cation calculated by means of the RCCSD(T) method are reported in Table 1 along with available experimental data provided by Ref. [40]. All structural and electric properties clearly exhibit smooth and very satisfactory convergence upon increasing the size of the basis set.

The theoretical values for $r_e$ obtained using the aug-cc-pV5Z and aug-cc-pV6Z basis sets agree within 0.0003 Å for both $CO^+(X^2\Sigma^+)$ and $CO^+(A^2\Pi)$. The exponential extrapolation for $r_e$ from the $X = 3 - 6$ data gives $r_e^\infty$ of 1.1166 Å and 1.2459 Å for $X^2\Sigma^+$ and $A^2\Pi$, respectively. These results are overestimated by about

Table 1. Geometric, spectroscopic, and electric properties of $CO^+(X^2\Sigma^+)$ and $CO^+(A^2\Pi)$ obtained by the RCCSD(T) method. The experimental data in the column denoted by Exp are taken from Refs. [40] and [42]. The theoretical $B_v$ values are computed as expectation values $\langle B\rangle_v$ of the rotational constant $B$ in the vibrational state $v$. The abbreviation aVXZ stands for the basis sets aug-cc-pVXZ. For additional information, see the main text.

| | $CO^+(X^2\Sigma^+)$ | | | | | $CO^+(A^2\Pi)$ | | | | |
|---|---|---|---|---|---|---|---|---|---|---|
| Property | aVTZ | aVQZ | aV5Z | aV6Z | Exp | aVTZ | aVQZ | aV5Z | aV6Z | Exp |
| $r_e$/A | 1.1225 | 1.1181 | 1.1170 | 1.1167 | 1.11514 | 1.2523 | 1.2473 | 1.2462 | 1.2459 | 1.24377 |
| $T_e/\mathrm{cm}^{-1}$ | | | | | | 19801 | 20254 | 20374 | 20417 | 20733.3 |
| $\tilde{\nu}_{1\leftarrow 0}/\mathrm{cm}^{-1}$ | 2164.7 | 2183.0 | 2186.2 | 2187.7 | | 1531.0 | 1539.3 | 1540.6 | 1541.4 | |
| $\tilde{\nu}_{2\leftarrow 0}/\mathrm{cm}^{-1}$ | 4300.2 | 4336.5 | 4342.8 | 4345.8 | | 3036.7 | 3053.1 | 3055.9 | 3057.5 | |
| $B_0/\mathrm{cm}^{-1}$ | 1.941 | 1.958 | 1.962 | 1.963 | 1.967465 | 1.560 | 1.572 | 1.574 | 1.575 | 1.5786 |
| $B_1/\mathrm{cm}^{-1}$ | 1.923 | 1.939 | 1.943 | 1.944 | | 1.541 | 1.554 | 1.555 | 1.556 | |
| $\langle r\rangle_0$/A | 1.127 | 1.122 | 1.121 | 1.121 | | 1.257 | 1.252 | 1.252 | 1.251 | |
| $\langle r\rangle_1$/A | 1.135 | 1.130 | 1.130 | 1.129 | | 1.269 | 1.264 | 1.263 | 1.263 | |
| $\omega_e/\mathrm{cm}^{-1}$ | 2192.9 | 2211.5 | 2214.7 | 2216.2 | 2214.2 | 1556.7 | 1565.0 | 1566.2 | 1566.9 | 1562.1 |
| $\omega_e x_e/\mathrm{cm}^{-1}$ | 13.800 | 13.887 | 13.935 | 13.938 | 15.164 | 12.874 | 12.922 | 12.862 | 12.835 | 13.532 |
| $\omega_e y_e/\mathrm{cm}^{-1}$ | -0.177 | -0.202 | -0.196 | -0.197 | | 0.039 | 0.043 | 0.045 | 0.043 | |
| $B_e/\mathrm{cm}^{-1}$ | 1.951 | 1.968 | 1.971 | 1.972 | 1.9772 | 1.569 | 1.582 | 1.583 | 1.584 | 1.5894 |
| $\alpha_e \times 10^2$ /$\mathrm{cm}^{-1}$ | 1.875 | 1.890 | 1.891 | 1.891 | 1.896 | 1.847 | 1.865 | 1.862 | 1.861 | 1.942 |
| $\mu_e/ea_0$ | 1.030 | 1.033 | 1.034 | 1.035 | | 0.315 | 0.310 | 0.309 | 0.309 | |
| $\Theta_{zz}/ea_0^2$ | 1.904 | 1.894 | 1.890 | 1.890 | | 0.076 | 0.063 | 0.056 | 0.055 | |
| $\Theta_{xx}/ea_0^2$ | -0.952 | -0.947 | -0.945 | -0.945 | | -0.631 | -0.619 | -0.614 | -0.613 | |
| $\Theta_{yy}/ea_0^2$ | -0.952 | -0.947 | -0.945 | -0.945 | | 0.555 | 0.556 | 0.558 | 0.558 | |

0.002 A with respect to the experimental findings [40], as seen in Table 1. The effect of the double augmentation is found to be negligible for the geometric parameters of $CO^+$: the d-aug-cc-pVXZ results for $r_e$ are changed by less than 0.0001 A, for $\mu_z$ by less than $0.0001\,ea_0$, and for $\Theta_{zz}$ by less than $0.0004\,ea_0^2$ with respect to the aug-cc-pVXZ values for X=4-6.

The rovibrational energies of $CO^+(X^2\Sigma^+)$ and $CO^+(A^2\Pi)$ were calculated by a variational technique using a Laguerre function basis [44] by solving a set of radial problems with centrifugal potentials of the form $\hbar^2[J(J+1)-\Omega^2]/2\mu r^2$ for total electronic angular momentum $\Omega$=1/2 or 3/2 and reduced mass $\mu$. Atomic masses without a correction for the missing electron were used and the lowest six rotational levels were computed. This leads to a theoretical set of $E_{vJ}$ eigenvalues and expectation values $\langle B\rangle_v$ and $\langle r\rangle_v$ (see Table 1) for rovibrational states. The two electronic states were treated separately without accounting for the above mentioned higher order couplings and our results should be compared to the deperturbed parameters obtained from experiments (see below). The differences between transition frequencies and expectation values obtained for the physically appropriate values of $\Omega = 1/2$ or 3/2 or using $\Omega = 0$ are actually below the last decimal place given in Table 1. Conventional spectroscopic constants were obtained by fitting subsets of the energies $E_{vJ}$ converged to at least 0.01 $cm^{-1}$ with $0 \le v \le 3$ (24 levels) for the $^2\Sigma^+$ state and $0 \le v \le 4$ (30 levels) for the $^2\Pi$ state, respectively, to the standard term formula [45]

$$\begin{aligned} E_v/hc = {} & \omega_e(v+\frac{1}{2}) - \omega_e x_e(v+\frac{1}{2})^2 \\ & +\omega_e y_e(v+\frac{1}{2})^3 \\ & +B_e J(J+1) - \alpha_e(v+\frac{1}{2})J(J+1), \end{aligned} \tag{7}$$

where $\omega_e x_e$ and $\omega_e y_e$ are the first and second anharmonicity constants, respectively. The rms error of these fits is less than 0.001$cm^{-1}$ for the $^2\Pi$ state and less than 0.0003$cm^{-1}$ for the $^2\Sigma^+$ state.

Note that more recently reported experimental spectroscopic constants are given as $\omega_e = 2214.127$, $\omega_e x_e = 15.094$, $\omega_e y_e = -0.0117$, $B_e = 1.976941$, $\alpha_e = 0.018943$ $cm^{-1}$ for $CO^+(X^2\Sigma^+)$ [46] and as $\omega_e = 1561.806$, $\omega_e x_e = 13.4785$, $\omega_e y_e = 0.00865$, $B_e = 1.589392$, $\alpha_e = 0.019494$ $cm^{-1}$ for $CO^+(A^2\Pi)$ [47, 48]. From velocity modulation measurements [49], the fundamental band center $\nu_{1\leftarrow 0}$ of $CO^+(X^2\Sigma^+)$ is known to be at $2183.9193(10)\,cm^{-1}$.

In Table 1, the theoretical values of $B_e$ for both electronic states and $B_0$ for the ground electronic state agree within 0.005 $cm^{-1}$ (0.3%) with the experimental findings. For the vibrational ground state in the electronic $A^2\Pi$ state, the deperturbation analysis of Katayama and Welsh [42] gave a deperturbed $B_0$ value of 1.5786(2) $cm^{-1}$, whereas Coxon and Foster [41] found $B_0 = 1.57976(12)$ $cm^{-1}$. Our RCCSD(T)/aug-cc-pV6Z result from Table 1 agrees with both of these values also within 0.005 $cm^{-1}$ (0.3%). This observation and the good agreement between the RCCSD(T) and MRCI curves, displayed in Figure 2, show that the RCCSD(T) method provides a reliable zero-order picture for both electronic states of $CO^+$. In the CASPT2 and MRCI calculations with the aug-cc-pVQZ basis set, the equilibrium C-O distance $r_e$ is calculated to be respectively 1.1211 and 1.1197 A for $CO^+(X^2\Sigma^+)$, whereas $r_e$ values of 1.2496 and 1.2482 A are obtained for $CO^+(A^2\Pi)$. The energy separation $T_e$ between the electronic states is found to be 21439 $cm^{-1}$ for CASPT2 and 20509 $cm^{-1}$ for MRCI; to be compared with the RCCSD(T)/aug-

cc-PVQZ result $T_e = 20254$ cm$^{-1}$.

An exponential extrapolation from the $X = 3{-}6$ data gives for $[\mu_z, \Theta_{zz}]$ the values $[1.0356\, ea_0, 1.8885\, ea_0^2]$ for $CO^+(X^2\Sigma^+)$ and $[0.3087\, ea_0, 0.0546\, ea_0^2]$ for $CO^+(A^2\Pi)$. For the latter state, the CBS values of $\Theta_{xx}$ and $\Theta_{yy}$ are estimated to be respectively -0.6130 and $0.5584\, ea_0^2$ for one of the two $A^2\Pi$ components and 0.5584 and -0.6130 $ea_0^2$ for the other. The quadrupole products $\Theta_{xy}$, $\Theta_{yz}$, and $\Theta_{zx}$ are all equal to zero due to symmetry. Linear molecules with nonzero electronic angular momentum possess cylindrically asymmetric charge density distributions [50]. In spatially degenerate $\Pi$ states, one dipole moment $\mu_z$ and two independent quadrupole moment terms exist: the parallel component $\Theta_{\|} = \Theta_{zz}$ and the anisotropy $\delta\Theta = |\Theta_{xx} - \Theta_{yy}|$. The perpendicular moments $\Theta_{xx} = -(\Theta_{zz} + \delta\Theta)/2$ and $\Theta_{yy} = -(\Theta_{zz} - \delta\Theta)/2$ are, thus, equidistant from the reference value $-\Theta_{zz}/2$. In $\Sigma$ states which have cylindrically symmetric charge density distributions, $\Theta_{xx} = \Theta_{yy} = -\Theta_{zz}/2$ holds.

Thompson *et al.* [51] used cyclotron frequency shifts arising from polarization forces to measure the quantum state of $CO^+$ and to estimate the corresponding dipole moment. Our theoretical prediction for $\mu_e$ of 1.035 $ea_0$ for $CO^+(X^2\Sigma^+)$ is in excellent agreement with their result $\mu = 1.025(15)$ $ea_0$, where the number in parentheses shows the standard uncertainty on the last two digits.

The equilibrium dipole moment of 1.035 $ea_0$ (2.6 D) for $CO^+$ in the ground electronic state is large and more than three times larger than $\mu_e$ of the $A^2\Pi$ state, as seen in Table 1. At the CCSD(T)/aug-cc-pVQZ level of theory, the equilibrium dipole moments of isoelectronic CN and of neutral CO are computed to be respectively $0.556\, ea_0$ and -0.042 $ea_0$. In all our calculations, the carbon atom was placed on the positive $z$ axis, such that $\mu_e$(CO) carries a negative sign due to the polarity $C^-O^+$ of neutral carbon monoxide (compare with Ref. [52]). The experimentally derived values of $|\mu_e|$ are $0.043\, ea_0$ for CO (Ref. [53]) and 1.45(8) D ($0.57\, ea_0$) for CN (Ref. [54]). For $\Theta_{zz}$ we obtain $-1.53\, ea_0^2$ for CO and $0.43\, ea_0^2$ for CN. It is noted that our RCCSD(T)/aug-cc-pVQZ values for $r_e$(CO) of 1.132 Å and $r_e$(CN) of 1.175 Å are in good agreement with the experimental results of respectively 1.128 Å and 1.172 Å given in Ref. [40].

Martin and Fehér [55] calculated CASSCF dipole and quadrupole moments as a function of the internuclear distance for the $X^2\Sigma^+$ and $A^2\Pi$ states of $CO^+$. The ground vibrational state values for $[\mu_z, \Theta_{zz}]$ reported there are $[1.015\, ea_0, 1.913\, ea_0^2]$ for the ground electronic state and $[0.297\, ea_0, 0.168\, ea_0^2]$ for the excited electronic state. In addition these authors also showed that the quadrupole moment $\Theta_{zz} = 1.03 \pm 0.07$ $ea_0^2$ for $CO^+(X^2\Sigma^+)$ obtained from earlier multiphoton excitation experiments [56] is too small. Our result for $\Theta_{zz}$ of $CO^+(X^2\Sigma^+)$ agrees within 0.02 $ea_0^2$ with the theoretical value of Martin and Fehér.

For $CO^+(A^2\Pi)$, our RCCSD(T) result $\Theta_{zz} = 0.055$ $ea_0^2$ appears about three times smaller than the vibrationally averaged value of $0.168\, ea_0^2$ reported previously [55]. To clarify this difference, we investigated the results of Ref. [55] in more detail. We fitted the potential energy $V$, the dipole moment $\mu_z$, and the quadrupole moment $\Theta_{zz}$ values from Table 1 of Ref. [55] to three-term polynomials in the region around the potential energy minimum for both electronic states. From the polynomial representations of $V$, equilibrium distances $r_e^{MF}$ were calculated as $r_e^{MF}(^2\Sigma^+) = 1.1285$ Å and $r_e^{MF}(^2\Pi) = 1.2618$ Å. The equilibrium values for $\mu_z$ and $\Theta_{zz}$, derived at $r_e^{MF}$ from the respective fits, are shown in Table 2 together with the results from the RCCSD(T), CASSCF, CASPT2, and MRCI calculations carried out at $r_e^{MF}$. From the polynomial representations of $\Theta_{zz}$, we also calculated that $\Theta_{zz}$ becomes zero at $r = 0.67$ Å for $X^2\Sigma^+$ and at $r = 1.21$ Å for $A^2\Pi$. Since the latter distance is only 0.05 Å smaller than the equilibrium value $r_e^{MF}(^2\Pi)$, the decrease of $\Theta_{zz}$ from its equilibrium value of 0.203 $ea_0^2$ (Table 2) to 0.168 $ea_0^2$ upon

vibrational averaging (Ref. [55]) is easy to understand in terms of $\Theta_{zz}$ changing its sign in the coordinate range accessed by the ground vibrational state.

In the electronic $A^2\Pi$ state, the nuclear contribution and the electronic contribution to the total molecular quadrupole moment $\Theta_{zz}$ at distances around the potential energy minimum are comparable in magnitude, but of opposite signs. A high level of treatment of electronic correlation is required to properly account for this delicate situation. Table 2 shows that for $CO^+$ the performance of the RCCSD(T) method is far superiour to the CASSCF and CASPT2 approaches and appears comparable with MRCI. Another important aspect for the determination of the electric properties is the description of the $\Pi$ state(s) as such. We tested this by performing two-state CAS calculations after the restricted Hartree-Fock (RHF) step to obtain balanced orbitals used in the subsequent RCCSD(T) computation. In this fashion, we derived for the $A^2\Pi$ state RCCSD(T)/aug-cc-pVQZ values, in atomic units, for $[\mu_z; \Theta_{zz}, \Theta_{xx}, \Theta_{yy}]$ of $[0.335; 0.131, -0.659, 0.528]$ at $r_e^{MF}(^2\Pi)$ and of $[0.311; 0.069, -0.622, 0.553]$ at $r_e = 1.2473$ A. These results should be compared with the values of $[0.334; 0.125, -0.655, 0.530]$ from Table 2 and of $[0.310; 0.063, -0.619, 0.556]$ from Table 1, respectively. This shows that the standard procedure to use molecular orbitals from RHF calculations in the RCCSD(T) calculations provides dipole moment values accurate within 0.001 $ea_0$ and quadrupole moment components accurate within 0.006 $ea_0^2$ for $CO^+(^2\Pi)$.

The additional splitting due to the electron spin and orbital angular momentum interaction was considered here only at $r = r_e$. A MRCI/aug-cc-pVQZ calculation using the Breit-Pauli operator gave a spin-orbit splitting between the two components of the $A^2\Pi$ state of 118 $cm^{-1}$, in very good agreement with experimental findings of 117.5 $cm^{-1}$ [40] and 122 $cm^{-1}$ [41].

### 3.2. *Helium*

Helium possesses a small static electric dipole polarizability $\alpha$. The mass polarization, relativistic, and QED corrections were previously found to cancel out for He, giving $\alpha$(He) of 1.383191(2) $a_0^3$ (Ref. [57]). A value of 1.38312 $a_0^3$ was derived for $\alpha$(He) by Thakkar [58]. Inspection of Table 3 shows excellent agreement of our CCSD(T)/aug-cc-pVXZ results for $\alpha$(He) with these previous theoretical findings. Regarding the experimentally derived $\alpha$(He) values, we note that $\alpha$(He)=1.405 $a_0^3$ is obtained from dipole (e,e) energy-loss spectra, whereas values in the range from 1.383 to 1.395 $a_0^3$ are found by means of refractive index and dielectric constant data, as given in Ref. [59].

The quadrupole polarizability $C_{zz,zz}$ describes the quadrupole moment of He induced by the electric-field gradient. Judging from Table 3, $C_{zz,zz}$ is more sensitive than $\alpha$(He) on the basis set cardinal number X of the aug-cc-pVXZ family. Whereas $\alpha$ obtained for X=5 and X=6 differ by only 0.0002 $a_0^3$, the corresponding results for $C_{zz,zz}$ deviate by 0.18 $a_0^5$, *i.e.* by 8%. To further investigate the basis set saturation effect, we also tested the efficacy of the CCSD(T) method in conjunction with the doubly augmented correlation consistent series, d-aug-cc-pVXZ. As seen in Table 3, the d-aug-cc-pVXZ results exhibit a more balanced performance compared to aug-cc-pVXZ, indicating thus that the d-aug-cc-pVXZ series is essential for the determination of $C_{zz,zz}$(He) in connection with the CCSD(T) approach. Note that the d-aug-cc-pV6Z result $C_{zz,zz} = 2.437\, a_0^5$ differs by 0.008 $a_0^5$ from the theoretical estimate of 2.445 $a_0^5$ reported previously [58, 60].

Table 2. Dipole moment $\mu_z$ and quadrupole moments $\Theta_{xx}, \Theta_{yy}, \Theta_{zz}$ for $CO^+(X^2\Sigma^+)$ and $CO^+(A^2\Pi)$ calculated at $r_e^{MF}(^2\Sigma^+) = 1.1285\,\text{A}$ and $r_e^{MF}(^2\Pi) = 1.2618\,\text{A}$ with the RCCSD(T), CASSCF, CASPT2, and MRCI methods and the aug-cc-pVQZ basis set. The values in the column labelled FitMF are derived from the results of Martin and Fehér [55] using polynomial fits of their original data. The anisotropy $\delta\Theta$ is defined as $\mid \Theta_{xx} - \Theta_{yy} \mid$.

| | $CO^+(X^2\Sigma^+)$ | | | | | $CO^+(A^2\Pi)$ | | | | |
|---|---|---|---|---|---|---|---|---|---|---|
| Property | FitMF | CASSCF | CASPT2 | MRCI | RCCSD(T) | FitMF | CASSCF | CASPT2 | MRCI | RCCSD(T) |
| $\mu_e/ea_0$ | 1.017 | 1.041 | 1.016 | 1.033 | 1.037 | 0.308 | 0.210 | 0.213 | 0.310 | 0.334 |
| $\Theta_{zz}/ea_0^2$ | 1.938 | 2.200 | 1.961 | 1.980 | 1.944 | 0.203 | -0.110 | -0.003 | 0.093 | 0.125 |
| $\Theta_{xx}/ea_0^2$ | | -1.100 | -0.980 | -0.990 | -0.972 | | -0.570 | -0.603 | -0.641 | -0.655 |
| $\Theta_{yy}/ea_0^2$ | | -1.100 | -0.980 | -0.990 | -0.972 | | 0.681 | 0.606 | 0.548 | 0.530 |
| $\delta\Theta/ea_0^2$ | | 0.0 | 0.0 | 0.0 | 0.0 | | 1.251 | 1.209 | 1.189 | 1.185 |

Table 3. Dipole polarizability $\alpha$ (in $a_0^3$) and quadrupole polarizability $C_{zz,zz}$ (in $a_0^5$) of helium obtained from the numerical differentiation of field/field-gradient dependent CCSD(T) energies. The induction coefficients $D_5/\cos\theta$ (in $ea_0^4$), defined by Eq. (13), are obtained from the respective $\mu_e(CO^+)$ values of Table 1. The values of $D_5/\cos\theta$ given in parentheses are evaluated using $\mu(CO^+)$ computed at $r(CO)$=1.11783 A. The abbreviations aVXZ and daVXZ stand for aug-cc-pVXZ and d-aug-cc-pVXZ, respectively.

| Basis | $\alpha$ | $C_{zz,zz}$ | $D_5/\cos\theta$ |
|---|---|---|---|
| aVTZ | 1.3793 | 1.358 | 2.8413 |
| | | | (2.8373) |
| aVQZ | 1.3842 | 1.791 | 2.8593 |
| | | | (2.8589) |
| aV5Z | 1.3830 | 2.052 | 2.8614 |
| | | | (2.8619) |
| aV6Z | 1.3828 | 2.233 | 2.8630 |
| | | | (2.8638) |
| daVTZ | 1.3885 | 2.356 | (2.8526) |
| daVQZ | 1.3852 | 2.420 | (2.8613) |
| daV5Z | 1.3828 | 2.432 | (2.8617) |
| daV6Z | 1.3827 | 2.437 | (2.8636) |

## 4. Ionic complex He-$CO^+$

The interaction with a helium atom leads to a floppy system with $C_s$ point group symmetry in which the $^2\Sigma^+$ state of $CO^+$ correlates with a $^2A'$ state and the $^2\Pi$ state is expected to split into a Renner-Teller coupled pair of $^2A'$ and $^2A''$ states. Spin-orbit coupling effects were not included at the present level of treatment but will be an important part of a more refined study of the electronically excited system.

The parameters calculated by the RCCSD(T) method for the ionic He-$CO^+$ complex in the ground $1^2A'$ and excited $1^2A''$ electronic states are collected in Table 4. Note that within the coupled cluster technique only the $A''$ component of the $^2\Pi$ state is accessible for non-linear arrangements (point group $C_s$).

The complex He-$CO^+(1^2A')$ in its ground electronic state has a nonlinear equilibrium structure defined by $(R_e, \theta_e) = (2.87\,\text{A}, 46^\circ)$ and an electronic binding energy of about 275 $cm^{-1}$. In the excited $1^2A''$ electronic state, the complex has $(R_e, \theta_e) = (2.92\,\text{A}, 78^\circ)$ and an electronic binding energy of about 160 $cm^{-1}$. For the neutral He-CO complex, dominated by dispersion interaction, Heijmen *et al.* [61] found a binding energy of only 23.734 $cm^{-1}$ and a bent equilibrium structure with $R_e = 3.46$ A and $\theta_e = 48.4^\circ$ when $r_e$(C-O)=1.128 A.

In addition to the geometric parameters $R_e, r_e, \theta_e$, Table 4 also provides the equilibrium rotational constants $A_e, B_e, C_e$ and Ray's asymmetry $\kappa$ parameter [62], where

$$\kappa = (2B_e - A_e - C_e)/(A_e - C_e). \tag{8}$$

In the bent molecule limit, the quasilinearity parameter $\gamma_0$ is given by [63]

$$\gamma_0 = 1 - 4A_e/\omega_3, \tag{9}$$

where $\omega_3$ is the harmonic bending frequency. The harmonic frequencies $\omega_1, \omega_2, \omega_3$, dipole moment components $\mu_i$, and molecular quadrupole moment tensor $\Theta_{ij}$ were

Table 4. Geometric, spectroscopic, and electric properties of He–$CO^+$ in the ground $1^2A'$ and excited $1^2A''$ electronic states obtained in RCCSD(T) calculations. For additional information, see the main text.

| | He–$CO^+(1^2A')$ | | | | He–$CO^+(1^2A'')$ | | | |
|---|---|---|---|---|---|---|---|---|
| Property | avdz | avtz | avqz | av5z | avdz | avtz | avqz | av5z |
| $r_e$/A | 1.1334 | 1.1224 | 1.1180 | 1.1169 | 1.2666 | 1.2523 | 1.2473 | 1.2462 |
| $R_e$/A | 3.0916 | 2.8901 | 2.8705 | 2.8677 | 2.9488 | 2.9253 | 2.9129 | 2.9160 |
| $\theta_e$/deg | 30.91 | 44.78 | 45.72 | 46.07 | 78.88 | 77.06 | 77.53 | 77.84 |
| $A_e/\mathrm{cm}^{-1}$ | 8.744 | 4.603 | 4.477 | 4.426 | 1.624 | 1.695 | 1.699 | 1.696 |
| $B_e/\mathrm{cm}^{-1}$ | 0.418 | 0.493 | 0.501 | 0.503 | 0.543 | 0.548 | 0.553 | 0.553 |
| $C_e/\mathrm{cm}^{-1}$ | 0.399 | 0.445 | 0.450 | 0.451 | 0.407 | 0.414 | 0.417 | 0.417 |
| $\kappa$ | -0.995 | -0.977 | -0.975 | -0.974 | -0.777 | -0.791 | -0.788 | -0.787 |
| $\omega_1/\mathrm{cm}^{-1}$ | 2155 | 2192 | 2212 | 2217 | 1499 | 1549 | 1562 | |
| $\omega_2/\mathrm{cm}^{-1}$ | 135 | 136 | 133 | 132 | 95 | 96 | 96 | |
| $\omega_3/\mathrm{cm}^{-1}$ | 42 | 50 | 47 | 48 | 44 | 40 | 42 | |
| $\gamma_0$ | 0.36 | 0.71 | 0.70 | 0.71 | 0.86 | 0.84 | 0.85 | |
| $\mu_z/ea_0$ | 1.096 | 1.083 | 1.085 | 1.086 | 0.336 | 0.322 | 0.316 | 0.315 |
| $\mu_x/ea_0$ | 0.047 | 0.069 | 0.071 | 0.071 | 0.051 | 0.052 | 0.053 | 0.053 |
| $\Theta_{zz}/ea_0^2$ | 2.323 | 2.000 | 1.970 | 1.959 | -0.127 | -0.152 | -0.167 | -0.174 |
| $\Theta_{xx}/ea_0^2$ | -0.984 | -0.687 | -0.663 | -0.655 | -0.212 | -0.160 | -0.146 | -0.142 |
| $\Theta_{yy}/ea_0^2$ | -1.339 | -1.313 | -1.307 | -1.304 | 0.338 | 0.311 | 0.313 | 0.315 |
| $\Theta_{zx}/ea_0^2$ | 0.535 | 0.560 | 0.557 | 0.555 | 0.118 | 0.142 | 0.137 | 0.132 |
| $T_e/\mathrm{cm}^{-1}$ | | | | | 19175 | 19917 | 20369 | 20488 |
| $E_{\mathrm{diss}}/\mathrm{cm}^{-1}$ | 310 | 286 | 281 | 278 | 178 | 169 | 167 | 164 |
| $E_{\mathrm{diss}}^{\mathrm{CP}}/\mathrm{cm}^{-1}$ | 217 | 251 | 269 | 274 | 135 | 150 | 158 | 161 |

determined with the RCCSD(T)/aug-cc-pVXZ approach at the respective equilibrium geometries.

Comparison of Tables 1 and 4 shows that the bond length of $CO^+$ remains nearly unaltered upon complex formation in both electronic states. The same is also true for the harmonic $\omega_1 = \omega(CO^+)$ frequency, which exhibits a small blue shift of about $1\,\mathrm{cm}^{-1}$ within this approximation. The energy separation $T_e$ between the electronic states is increased by about $115\ \mathrm{cm}^{-1}$ for $X = 3 - 5$ after complexation.

In Table 4, the electronic binding energies $E_{\mathrm{diss}}$ and $E_{\mathrm{diss}}^{\mathrm{CP}}$ were determined at equilibrium as $E_{\mathrm{diss}} = -E_{int}$ and $E_{\mathrm{diss}}^{\mathrm{CP}} = -E_{int}^{\mathrm{CP}}$, where the superscript CP refers to counterpoise corrected results. The binding between He and $CO^+(X^2\Sigma^+)$ is about $110\,\mathrm{cm}^{-1}$ stronger than for the $A''$ component of the interaction between He and $CO^+(A^2\Pi)$. The BSSE generally introduces a nonphysical attraction between monomers, such that CP corrections lead to a less stable complex and $E_{\mathrm{diss}}^{\mathrm{CP}}$ values smaller than the corresponding $E_{\mathrm{diss}}$ results. For the aug-cc-pVXZ series with X = 2-5, $E_{\mathrm{diss}}^{\mathrm{CP}}$ is lower than $E_{\mathrm{diss}}$ by 93, 35, 12, 4 $\mathrm{cm}^{-1}$ for $X^2\Sigma^+$ and by 43, 19, 9, 3 $\mathrm{cm}^{-1}$ for $A^2\Pi$, respectively, such that the residual BSSE effect is larger for the smallest basis set.

The RCCSD(T) minimum energy paths (MEP) along the Jacobi angle $\theta$ for several members of the aug-cc-pVXZ basis set family are shown in Figure 3. These MEPs are obtained by energy minimization with respect to both $R$ and $r$ at the CP uncorrected level. We may note that the CO bond length is effectively constant, exhibiting a variation of about 0.0001 A along each of the displayed MEPs. The CP

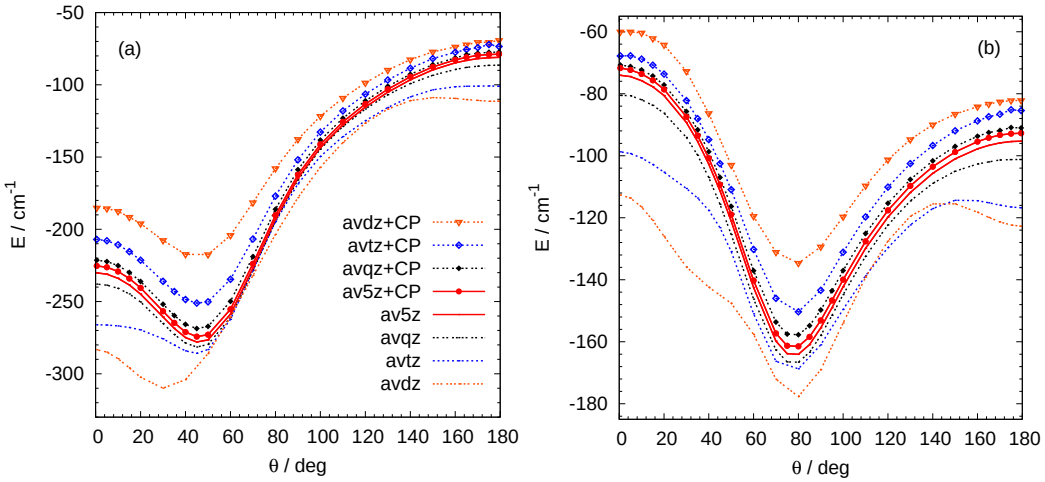


Figure 3. Minimum energy path in the direction of the Jacobi angle $\theta$ obtained by the RCCSD(T) method for the complex He-$CO^+$ in the ground $1^2A'$ electronic state (a) and in the excited $1^2A''$ electronic state (b). The zero energy is defined as the energy of infinitely separated He and $CO^+$. The aug-cc-pVXZ basis set label is abbreviated as aVXZ here and the line styles and labels apply to both parts (a) and (b) of this figure.

uncorrected and CP corrected angular MEPs clearly converge towards a common limit for both electronic states.

Along the CP corrected aug-cc-pV5Z angular MEP in Figure 3, the first and second linearization barriers at $\theta = 0°$ and $\theta = 180°$ are located at 49 $cm^{-1}$ and 195 $cm^{-1}$, respectively, above the minimum for He-$CO^+(1^2A')$, whereas they are at 90 and 70 $cm^{-1}$ for He-$CO^+(1^2A'')$. For both electronic states the angular anisotropy, *i.e.* the difference between the maximum and minimum along the angular MEP, is large (70% and 55% of the well depth).

The dipole moment $\mu_z$ is somewhat larger in the complex than in the $CO^+$ monomer for both electronic states, as seen in Tables 1 and 4. The $\mu_x$ components of 0.071 $ea_0$ for $1^2A'$ and of 0.053 $ea_0$ for $1^2A''$ at the RCCSD(T)/aug-cc-pV5Z level (Table 4) exceed the components $\mu_x^{\rm ind}$ expected to arise from the dipole induced on the He atom within the simple point-charge model, which amount to 0.034 and 0.045 $ea_0$, respectively. The dipole moment components were computed at the CP uncorrected level. The excellent convergence with respect to the basis set size observed for both $\mu_z$ and $\mu_x$ in Table 4 excludes a basis set superposition error as the origin of the observed enhancement.

The variation of the magnitude $|\mu|$ of the dipole moment vector with the Jacobi distance $R$ obtained in our RCCSD(T)/aug-cc-pVQZ calculations is shown in Figure 4 for the complex in its ground electronic state. The dipole exhibits a steep exponential increase at small separations (due to overlap effects) and varies very slowly at large separations (due to the electron correlation effects), approaching the free $CO^+$ limit from above. The dipole moment vector of the complex encloses a small angle (less than 4°) with the dipole moment vector of $CO^+$ for $R \geq R_e$. Compared to $\mu_e(CO^+)$, the dipole moment of the complex at equilibrium is enhanced by about 0.05 $ea_0$, see Tables 1 and 4. For $R = 15$ and 20 A, $|\mu|$ assumes values of respectively 1.0342 and 1.0338 $ea_0$, about 0.001 $ea_0$ larger than the equilibrium RCCSD(T)/aug-cc-pVQZ value of 1.033 $ea_0$ for free $CO^+(X^2\Sigma^+)$.

The $A'$ component of the $^2\Pi$ state for non-linear arrangements was explored with the CASPT2 method. After a restricted Hartree-Fock step, CASSCF calculations were performed for the three electronic states $1^2A'$, $2^2A'$, and $1^2A''$ using a set of nine active molecular orbitals with two doubly occupied core orbitals. This common orbital set was employed in subsequent three-state CASPT2 calculations. To

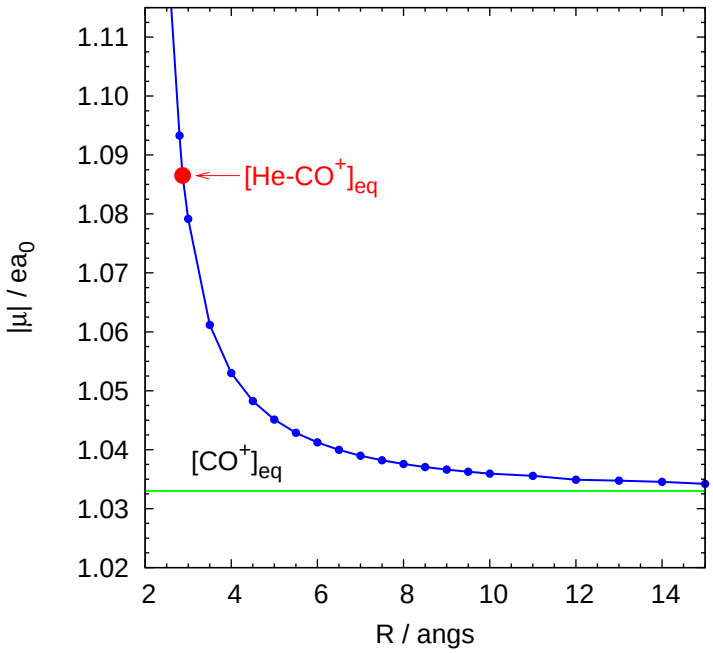


Figure 4. Variation of the magnitude $|\boldsymbol{\mu}|$ of the dipole moment vector with the Jacobi distance $R$ obtained for the He-$CO^+(1^2A')$ complex at the RCCSD(T)/aug-cc-pVQZ level. The remaining two coordinates $r, \theta$ are kept at their equilibrium values. The horizontal line at $\mu$=1.033 $ea_0$ shows the RCCSD(T)/aug-cc-pVQZ dipole moment calculated for free $CO^+(X^2\Sigma^+)$. The values of $|\boldsymbol{\mu}|$ corresponding to the complex at equilibrium is additionally shown.

provide a consistent data set, we summarize in Table 5 our CASPT2/aug-cc-pVTZ results for the three electronic states $1^2A'$, $2^2A'$, and $1^2A''$ of the complex.

Comparison of Table 5 and Table 4 for the electronic states $1^2A'$ and $1^2A''$ shows that the CASPT2/aug-cc-pVTZ and RCCSD(T)/aug-cc-pVTZ results for $r_e$, $R_e$, and $\theta_e$ agree within 0.003 $A$, 0.03 $A$, and 0.5°, respectively. The dipole and quadrupole moment components agree within 0.02 $ea_0$ and 0.07 $ea_0^2$, respectively. We also refer to Table 2, which indicates the importance of electronic correlation effects beyond the CASPT2 treatment for the correct evaluation of the electric properties.

For the quadrupole moment $\Theta$, the principal inertial axis tensor and the principal quadrupole axis tensor are given in Table 5 in addition to the components evaluated with respect to the $x, y, z$ reference frame of Figure 1. The principal axes $a, b, c$ of the moment-of-inertia tensor $I$ are defined such that $I_a \leq I_b \leq I_c$ holds for the eigenvalues of $I$. The results with respect to the inertial axis system are of spectroscopic interest. Diagonalization of the $\Theta$ tensor gives the principal quadrupole axes $\alpha, \beta, \gamma$ and the eigenvalues $\Theta_{\alpha\alpha}$, $\Theta_{\beta\beta}$, $\Theta_{\gamma\gamma}$, where $\Theta_{\alpha\alpha}$ is the major principal component chosen such that

$$| \Theta_{\alpha\alpha} | \geq | \Theta_{\beta\beta} | \geq | \Theta_{\gamma\gamma} | \, . \tag{10}$$

The angle between the axes/directions $p$ and $s$ is denoted by $\theta(p, s)$ in Table 5.

Inspection of Table 5 shows that the major principal components $\Theta_{\alpha\alpha}$ are all positive. The largest $\Theta_{\alpha\alpha}$ is found for the $1^2A'$ state. In addition, $\Theta_{\alpha\alpha}$ for $2^2A'$ is about three times bigger than $\Theta_{\alpha\alpha}$ for $1^2A''$. In the $A'$ states, the quadrupole axis $\alpha$ lies in the plane parallel to the molecular $z \wedge x$ plane, close to the $z$-axis (the bond-distance C-O vector $\mathbf{r}$) in the $1^2A'$ state and along the Jacobi vector $\mathbf{R}$ in the $2^2A'$ state, as indicated by the values of $\theta(z, \alpha)$ and $\theta(\mathbf{R}, \alpha)$, respectively. In the electronic $1^2A''$ state, the axis $\alpha$ is perpendicular to the molecular $z \wedge x$ plane.

Table 5. Geometric and electric parameters of the He-$CO^+$ complex in the electronic states $1^2A'$, $2^2A'$, and $1^2A''$ obtained from three-state CASPT2 calculations using the aug-cc-pVTZ basis set. For additional information, see the main text.

| State | $1^2A'$ | $2^2A'$ | $1^2A''$ |
|---|---|---|---|
| $r_e$ / A | 1.125 | 1.254 | 1.254 |
| $R_e$ / A | 2.922 | 2.415 | 2.947 |
| $\theta_e$/deg | 44.3 | 90.0 | 77.2 |
| $E_{\rm diss}$ / $\rm cm^{-1}$ | 263 | 349 | 158 |
| $E_{\rm diss}^{\rm CP}$ / $\rm cm^{-1}$ | 229 | 303 | 140 |
| $T_e/\rm cm^{-1}$ | | 20832 | 21023 |
| $\mu_z$ / $ea_0$ | 1.066 | 0.191 | 0.206 |
| $\mu_x$ / $ea_0$ | 0.058 | 0.080 | 0.049 |
| $\Theta_{zz}$ / $ea_0^2$ | 2.048 | -0.357 | -0.253 |
| $\Theta_{xx}$ / $ea_0^2$ | -0.758 | 1.232 | -0.139 |
| $\Theta_{yy}$ / $ea_0^2$ | -1.290 | -0.875 | 0.392 |
| $\Theta_{zx}$ / $ea_0^2$ | 0.493 | -0.023 | 0.137 |
| $\mu_a$ / $ea_0$ | 0.894 | 0.080 | 0.115 |
| $\mu_b$ / $ea_0$ | -0.583 | 0.191 | 0.178 |
| $\Theta_{aa}$ / $ea_0^2$ | 1.537 | 1.232 | -0.066 |
| $\Theta_{bb}$ / $ea_0^2$ | -0.248 | -0.357 | -0.326 |
| $\Theta_{cc}$ / $ea_0^2$ | -1.290 | -0.875 | 0.392 |
| $\Theta_{ac}$ / $ea_0^2$ | -1.190 | -0.023 | 0.072 |
| $\theta(z,a)$/deg | 36.2 | 90.0 | 70.8 |
| $\theta(\mathbf{R},a)$/deg | 8.1 | 0.0 | 6.4 |
| $\Theta_{\alpha\alpha}$ / $ea_0^2$ | 2.132 | 1.232 | 0.392 |
| $\Theta_{\beta\beta}$ / $ea_0^2$ | -1.290 | -0.875 | -0.344 |
| $\Theta_{\gamma\gamma}$ / $ea_0^2$ | -0.842 | -0.357 | -0.047 |
| $\theta(z,\alpha)$/deg | 170.3 | 90.8 | 90.0 |
| $\theta(z,\beta)$/deg | 90.0 | 90.0 | 56.3 |
| $\theta(\mathbf{R},\alpha)$/deg | 145.4 | 179.2 | 90.0 |
| $\theta(\mathbf{R},\beta)$/deg | 90.0 | 90.0 | 69.2 |

The ionic complex He-$CO^+$ in its $2^2A'$ state possesses a T-shaped equilibrium structure, with a Jacobi distance $R_e$ which is about 0.5 A shorter than $R_e$ for the other two states. Among the three states shown in Table 5, the $2^2A'$ state is the most strongly bound. The counterpoise corrected angular minimum energy paths for the excited electronic states $2^2A'$ and $1^2A''$ at the CASPT2 level are compared in Figure 5. These two profiles will clearly support different numbers of bound states.

## 5. Intermolecular potential

Buckingham [64] showed that the long range contribution to intermolecular potentials can be obtained from second order perturbation theory. In the case of He-$CO^+$ the induction (polarization) energy arising from the permanent moments of $CO^+$

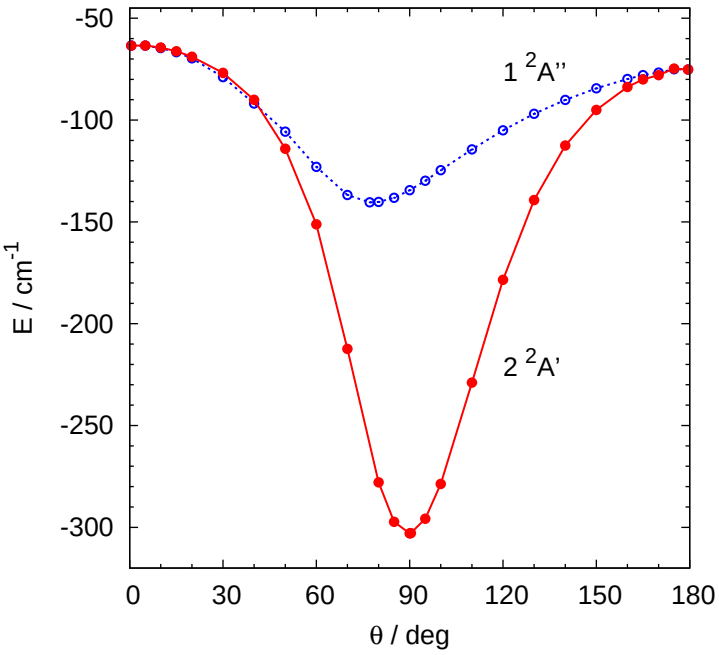


Figure 5. Minimum energy paths along the Jacobi angle $\theta$ obtained for the He-$CO^+$ complex in the electronic states $1^2A''$ and $2^2A'$ at the CASPT2/aug-cc-pVTZ level.

is derived from the general results of Ref. [64] to be

$$V_{ind}(\theta, R) = -D_4\, R^{-4} - D_5\, R^{-5} - D_6\, R^{-6} \cdots , \tag{11}$$

where

$$2\, D_4 = \alpha\, q^2, \tag{12}$$

$$D_5 = 2\, \alpha\, q\, \mu \cos\theta, \tag{13}$$

$$\begin{aligned} 2D_6 = {} & 3\alpha\, q\, \Theta_{zz}\, (3\cos^2\theta - 1) \\ & + \alpha\, \mu^2\, (3\cos^2\theta + 1) \\ & + \frac{3}{4} C_{zz,zz}\, q^2\, (9\cos^4\theta - 9\cos^2\theta + 4). \end{aligned} \tag{14}$$

In the above equations, $\alpha$ and $C_{zz,zz}$ refer to the helium dipole polarizability and the helium quadrupole polarizability, respectively, whereas $q$, $\mu$, and $\Theta_{zz}$ stand for the charge, the dipole moment, and the quadrupole moment of $CO^+$.

The leading long range term in the expansion of Eq. (11) for $V_{ind}$ is the charge-induced dipole contribution, which is isotropic and of $R^{-4}$ dependence. The dipole-induced dipole part varying as $R^{-5}$ clearly favours linear arrangements of the complex. The last term in Eq. (11) with $R^{-6}$ dependence prefers T-shaped forms since $\partial D_6/\partial\theta \sim \sin 2\theta$. In addition to the induction contribution of Eq. (11), there is also the dispersion contribution to the interaction energy, which is anisotropic with a leading $R^{-6}$ dependence. More details and the explicit angular dependence of this contribution are given in Ref. [64].

In view of Eq. (12), the induction coefficient $D_4$ equals to $\alpha/2$ for He-$CO^+$. The coefficients $D_5$ summarized in Table 3 are obtained with the help of Eq. (13), employing the results for $\mu_e(CO^+)$ and $\alpha$(He) from Tables 1 and 3. The parts $3\alpha q\Theta_{zz}$, $\alpha\mu^2$, and $3C_{zz,zz}q^2/4$ are respectively 7.84, 1.48, and 1.67 a.u. at the aug-cc-pV6Z

level, such that the coefficient $D_6$ of Eq. (14) assumes values of about 28 a.u. for $\theta = 0, 180^\circ$ and of 0.3 a.u. for $\theta = 90^\circ$.

The coefficient $D_5$ of Eq. (13) is directly related to the coefficient $C_5$ defined by Eq. (6) in Ref. [27]. The difference in the signs of $D_5$ and $C_5$ is due to the fact that the dipole moment vector $\boldsymbol{\mu}(CO^+)$ and the diatom distance vector $\boldsymbol{r}$ have opposite directions for the coordinate system adopted in Ref. [27] and the same direction in our convention of Figure 1.

### 5.1. *Potential energy surface for the ground electronic state*

In the present work, global potential energy surfaces are constructed for the ionic complex He($^1S$)-$CO^+$($^2\Sigma^+$) in the ground electronic state only. The zero of the energy scale is defined as the energy of He and $CO^+$($^2\Sigma^+$) at infinite separation.

In order to produce a complete potential energy representation, the interaction energies were evaluated over a large range of intermolecular configurations. For the angular grid, we chose 13 values of $\theta$ at 0° (15°) 180°, where the number in parentheses gives the increment. For $R$, we chose 28 values at 2.2 (0.1) 3.6 (0.2) 4.0 (0.25) 4.5 (0.5) 6.0 (1.0) 8.0, 10.0, 12.5, 15.0, 20.0 A. For a chosen $r$ value, the $(R, \theta)$ grid therefore contains 364 *ab initio* points.

The two-dimensional potential energy surfaces were constructed by treating $CO^+$ as a rigid entity. In these calculations, we chose $r = r_0(CO^+) = 1.11783$ A and $r = r_1(CO^+) = 1.12325$ A. These values were derived from the experimental values for $B_e$ and $\alpha$ quoted in Table 4 within the approximation $B_v \approx \hbar^2/(2\mu r_v^2)$. With $m(^{16}O) = 15.99491463$ a.m.u. the reduced mass $\mu$ for $^{12}C^{16}O^+$ is 6.8562086 a.m.u. The resulting $B_0 = B_e - \frac{1}{2}\alpha$ value is 1.96772 $cm^{-1}$ and corresponds to an effective $r_0(CO)$ of 1.11783 A. The value for $B_1 = B_e - \frac{3}{2}\alpha$ is 1.94876 $cm^{-1}$ and yields an effective $r_1(CO)$ of 1.12325 A. *Ab initio* computations were carried out using the basis sets aug-cc-pVXZ with X=2-5. The interaction energies at the complete basis set limit were estimated by means of the two-step procedure described by Eqs. (3)-(6). The calculated interaction energies were in the range from -275 $cm^{-1}$ to approximately 5150 $cm^{-1}$ and are all included in the fitting procedure.

### 5.2. *Least-squares fit: two-dimensional case*

The two-dimensional $(R, \theta)$ grid of the *ab initio* interaction energies are fitted to the two-dimensional analytical expression

$$V(R,\theta) = e^{-b[R-R^{ref}(\theta)]} \sum_{k=0}^{3} A_k(\theta) R^k \qquad (15)$$

$$-\frac{1}{2}[1+\tanh(R)] \sum_{k=4}^{8} C_k(\theta) R^{-k}$$

with the angle dependent parameters $A_k(\theta)$, $R^{ref}(\theta)$, and $C_k(\theta)$ given by the Legendre expansion

$$X_k = \sum_{l=0}^{n_X} X_{kl} P_l(\cos\theta), \qquad (16)$$

where $X$ stands for $A_k$, $R^{ref}$, or $C_k$, and $P_l(x)$ are Legendre polynomials in $\cos\theta$.

Table 6. Expansion coefficients $A_{kl}$, $C_{kl}$, and $R_l^{ref}$ (in atomic units) of Eq. (15) for the extrapolated RCCSD(T) potential energy surface derived in this work for He-$CO^+$ in its ground electronic state. The parameters $C_{40}$ and $C_{51}$ are constrained at the values of 0.692 $a_0^4$ and 2.86 $a_0^5$, respectively. The parameter $b$ assumes a value of 2.1785692 $a_0^{-1}$.

| $l$ | $A_{0l}$ | $A_{1l}$ | $A_{2l}$ | $A_{3l}$ | $C_{6l}$ | $C_{7l}$ | $C_{8l}$ | $R_l$ |
|---|---|---|---|---|---|---|---|---|
| 0 | -15.300904 | 10.149098 | -1.5520637 | 0.0566219 | 6.7877300 | 92.530248 | -389.36898 | 1.3719015 |
| 1 | 28.007617 | -19.139516 | 3.7663250 | -0.2382099 | 33.917847 | -477.33945 | 1724.7664 | 0.5347318 |
| 2 | -0.8674616 | 1.3654392 | -0.4326854 | 0.0468597 | 16.635297 | -100.03706 | 496.08775 | 0.6515154 |
| 3 | -2.9119325 | 1.6561188 | -0.3780590 | 0.0299295 | 5.3562451 | -104.03100 | 511.90542 | 0.0758250 |
| 4 | -0.3099230 | 0.6359557 | -0.1605319 | 0.0095310 | 1.2089629 | -30.883459 | 133.94147 | |

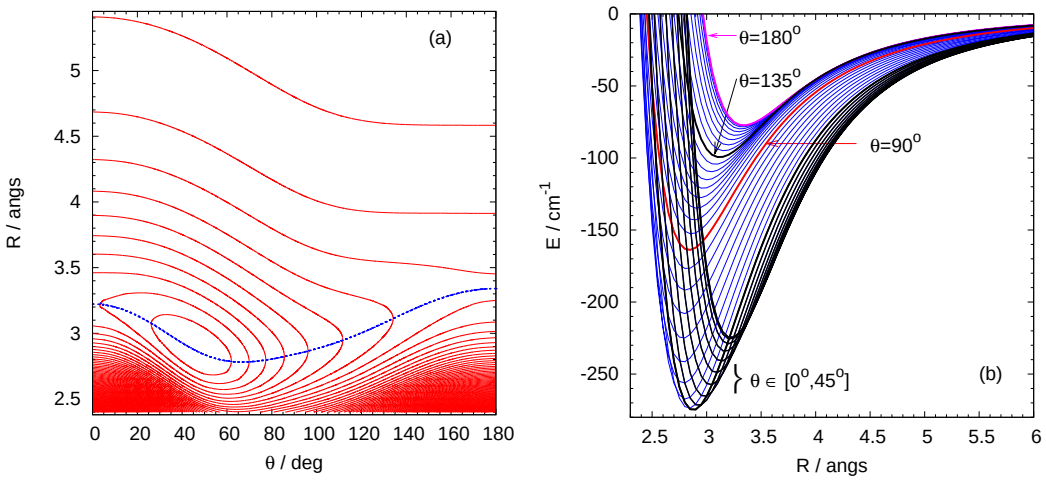


Figure 6. Contour plot of the RCCSD(T)/aug-cc-pV∞Z potential energy surface (a) and potential cuts along the Jacobi distance $R$ for chosen $\theta$ values (b) for the complex He-$CO^+$ in the ground electronic state. The energy interval between contours is 25 $cm^{-1}$ with the first contour drawn at -250 $cm^{-1}$. The dotted line on the contour map represents the minimum energy path in the direction of the Jacobi angle $\theta$.

The functional form of Eq. (15) was found to be very efficient and easy for fitting purposes, as previously demonstrated in a study of the $C_2H_2^+$-Ar complex [65].

The parameter $n_X$ in Eq. (16) is chosen to be 4 for $A_k$ and $C_k$ and 3 for $R^{ref}$. In the final fitting, we assume isotropic $R^{-4}$ and $\cos\theta$ angle dependent $R^{-5}$ contributions in agreement with Eq. (11). In other words, $C_{4l}$ for $l = 1-4$ and $C_{5l}$ for $l = 0, 2-4$ were all set to zero. For the parameters $C_{40}$ and $C_{51}$, we chose the respective theoretical values of $D_4$ and $D_5$, provided by Table 3. We employed a nonlinear least-squares technique (Levenberg-Marquardt algorithm) [66] and unweighted fitting procedure to find optimum values of the free parameters. The functional form of Eq. (15) is used to fit each of the RCCSD(T)/aug-cc-pVXZ *ab initio* point sets for X=2-5 and for the interaction energies extrapolated to the complete basis set limit (X=∞). The parameters $A_{kl}$, $C_{kl}$, and $R_l^{ref}$ for the latter RCCSD(T)/aug-cc-pV∞Z potential energy surface are summarized in Table 6. The standard deviation of the 42-term expansion was about 0.2 $cm^{-1}$. For bound (negative) energies, a maximum deviation of 0.4 $cm^{-1}$ was found for an energy at about -135 $cm^{-1}$, whereas deviations smaller than 0.1 $cm^{-1}$ were seen in the long range.

The RCCSD(T)/aug-cc-pV∞Z potential energy surface is graphically displayed in Figure 6. Along the angular minimum energy path, the optimum intermolecular

Table 7. Selected results for He-$CO^+(1^2A')$ from the rovibrational DVR-DGB calculations with the two-dimensional RCCSD(T)/aug-cc-pVXZ potential energy surfaces, constructed using the C-O bond lengths $r_0$ = 1.11783 A and $r_1$ = 1.12325 A for rigid $CO^+$. In addition to the vibrational ground-state energy $E_0$, the ground-state rotational constants $A_0, B_0, C_0$, and the fundamental bending $\nu_b$ and stretching $\nu_s$ frequencies, we also give the equilibrium geometry $R_e, \theta_e$ and the energy $V_{\rm min}$ at the minimum obtained by the minimization of the corresponding potential energy surface. The asymmetry parameter $\kappa$ and the quasilinearity parameter $\gamma_0$ are defined by Eqs. (8) and (9). The abbreviations aVXZ and $aVXZ_{corr}$ denote PESs based on the CP uncorrected and CP corrected interaction energies from the RCCSD(T)/aug-cc-pVXZ calculations.

| | $r = r_0$ | | | | | | | $r = r_1$ |
|---|---|---|---|---|---|---|---|---|
| Property | aVTZ | $aVTZ_{corr}$ | aVQZ | $aVQZ_{corr}$ | aV5Z | $aV5Z_{corr}$ | aV∞Z | aV∞Z |
| $R_e$/A | 2.898 | 2.905 | 2.870 | 2.878 | 2.868 | 2.871 | 2.866 | 2.870 |
| $\theta_e$/deg | 43.8 | 46.2 | 45.8 | 46.0 | 46.1 | 46.1 | 46.2 | 46.1 |
| $V_{\rm min}/{\rm cm}^{-1}$ | -285.8 | -252.4 | -281.6 | -269.0 | -277.7 | -274.0 | -275.3 | -274.5 |
| $E_0/{\rm cm}^{-1}$ | -209.7 | -177.5 | -201.3 | -189.9 | -197.6 | -194.2 | -195.0 | -194.6 |
| $A_0/{\rm cm}^{-1}$ | 10.3 | 7.315 | 7.679 | 7.328 | 7.362 | 7.256 | 7.207 | 7.186 |
| $B_0/{\rm cm}^{-1}$ | 0.444 | 0.454 | 0.462 | 0.462 | 0.465 | 0.465 | 0.467 | 0.465 |
| $C_0/{\rm cm}^{-1}$ | 0.395 | 0.400 | 0.408 | 0.407 | 0.410 | 0.409 | 0.410 | 0.409 |
| $\nu_b/{\rm cm}^{-1}$ | 31.9 | 32.8 | 34.3 | 34.4 | 34.7 | 34.7 | 35.0 | 34.8 |
| $\nu_s/{\rm cm}^{-1}$ | 94.8 | 86.5 | 94.2 | 91.3 | 93.6 | 92.8 | 93.3 | 93.2 |
| $\kappa$ | -0.990 | -0.984 | -0.985 | -0.984 | -0.984 | -0.984 | -0.983 | -0.983 |
| $\gamma_0$ | -0.31 | 0.08 | 0.08 | 0.12 | 0.12 | 0.14 | 0.15 | 0.17 |

distance varies between 2.8 A ($\theta \approx 65°$) and 3.4 A ($\theta = 180°$). The radial profiles seen in Figure 6(b) show a minimum at distances $R$ larger than $R_e$ for $\theta < \theta_e$ and at $R$ smaller than $R_e$ for $\theta > \theta_e$. Their curvature and the respective binding energy exhibit pronounced angular dependences, indicating, thus, prominent angular-radial coupling.

## 6. Bound state calculations

Bound rovibrational levels of He-$CO^+(1^2A')$ were calculated with the help of the DVR-DGB method [65, 67], which uses a discrete variable representation (DVR) for the angular coordinate and a distributed Gaussian basis (DGB) for the radial degree of freedom. We chose 50 Gauss-Legendre DVR points in $\theta$. The radial basis included up to 80 angle dependent Gaussian functions distributed non-evenly between $4\,a_0$ and $300\,a_0$. The rovibrational levels of the complex were calculated for the total rotational angular momentum $J$ as high as $J$=10 in both parities.

Selected results from the DVR-DGB calculations are summarized in Table 7 for several of the potential energy surfaces described above. There we also give the geometric parameters $R_e, \theta_e$ and the energy $V_{\rm min}$ at the minimum, obtained by minimizing the potential energy functions. It is to be noted that the equilibrium geometry $R_e, \theta_e$ for the CP uncorrected 2D PESs in Table 7 may differ slightly from the corresponding values given in Table 4 since the results of Table 7 are obtained keeping $r$(CO) constant.

The vibrational ground state $E_0$ lies about $80\,{\rm cm}^{-1}$ above the respective potential minimum and is bound by $195\,{\rm cm}^{-1}$, as seen from the RCCSD(T)/aug-cc-pV∞Z results in Table 7. The fundamental bending $\nu_b$ transition of $35\,{\rm cm}^{-1}$ and the fundamental stretching $\nu_s$ transition of $93\,{\rm cm}^{-1}$ are lower by respectively 13 and $39\,{\rm cm}^{-1}$ than their harmonic counterparts from Table 4. Comparison of the results obtained

for $r(\mathrm{CO})=r_0$ and $r(\mathrm{CO})=r_1$ shows a rather small effect of the elongation of $r$ on the quantities summarized in Table 7.

The ground state rotational constants $A_0, B_0, C_0$ in Table 7 are evaluated from $J = 0, 1$ results. Note that the result for $A_0$ appears significantly different from the corresponding equilibrium value $A_e$ reported in Table 4. In view of the asymmetry parameter $\kappa$ of -0.98, the rotation of the complex approaches the prolate symmetric top limit. Judging from the quasilinearity parameter $\gamma_0$, the rovibrational dynamics is expected to approach the bent-molecule limit at equilibrium due to $\gamma_0 \approx 0.7$ (Table 4) and to become more quasilinear after vibrational averaging due to $\gamma_0 \approx 0.1$ (Table 7).

The complex has 19 bound $J = 0$ states. The number of bound odd-parity $J = 1$ states is 16, taking into account that the energy $E[\mathrm{CO}^+(j = 1)]$ amounts to 3.935 $\mathrm{cm}^{-1}$. The number of bound states increases with $J$ since $K > 0$ levels become accessible for $J > 0$.

The rovibrational levels of He-$\mathrm{CO}^+$ were analysed in detail by means of the adiabatic projection scheme based on the adiabatic bend approximation. This type of analysis enabled us to characterize the rovibrational levels and to study the relevance of the intermode coupling (vibrational mixing) and the rotation-vibration mixing. For more detail on adiabatic projection schemes in combination with the DVR approach, see Ref. [68].

The full-dimensional rovibrational energies are denoted by $E^{(J,p)}$ and the corresponding ordinal numbers by $n^{(J,p)}$ for a given total rotational angular momentum $J$ and parity $p$. The quantum number labels are given as $(v_b, v_s; K)$ or as $(v_b, v_s)$ when $K = 0$, where $v_b, v_s$ specify the state of the intermolecular bend $\nu_b$ and the intermolecular stretch $\nu_s$, and $K$ is the quantum number for the body-fixed $z$-projection of $J$. In the DVR-DGB calculations, the body-fixed $z$-axis was defined to lie along the Jacobi vector $\mathbf{R}$. The direction of $\mathbf{R}$ is a good approximation for the principal moment of inertia axis of the complex He-$\mathrm{CO}^+$ since we found that the true principal axis departs by only a few degrees (at most 8°) from $\mathbf{R}$ along the minimum energy path.

### 6.1. *Vibrational structure*

The effective adiabatic bend profiles $V_{\mathrm{adi}}^{v_s}$ together with the minimum energy path $V_{\mathrm{MEP}}$ are shown in Figure 7. The angular profiles $V_{\mathrm{adi}}^{v_s}$ are obtained by adding to the bare MEP the energy $\varepsilon_{v_s}$ of the intermolecular stretching vibration in the state $v_s$, computed at the chosen angular DVR points. The effective one-dimensional vibrational spacings $\Delta_{v_s}$ in the state $v_s$, obtained as

$$\Delta_{v_s} = (\varepsilon_{v_s} - \varepsilon_0)/v_s \tag{17}$$

at a given Jacobi angle, are displayed in Figure 8.

Upon excitation of the one-dimensional stretching mode, the effective profiles $V_{\mathrm{adi}}^{v_s}$ in Figure 7 become shallower, resulting in smaller binding energies for higher $v_s$. In return, the adiabatic bending transition $\omega_b^{adi}$ shows a strong dependence on stretching excitation, as seen from adiabatic $\omega_b^{adi}$ that are computed to be 37, 30, 24, 15 $\mathrm{cm}^{-1}$ for $v_s = 0$, 1, 2, 3, respectively. The separation between the adjacent $V_{adi}^{v_s}$ profiles is non-uniform along the bending angle. In Figure 8, we see that the effective vibrational spacing of the intermolecular stretch assumes the largest value in the region of the potential energy minimum and is reduced by about $10\,\mathrm{cm}^{-1}$ when $\theta \to 0°$ and by about 40-50 $\mathrm{cm}^{-1}$ when $\theta \to 180°$ with respect to the value at $\theta_e$. These results reflect a strong stretch-bend coupling and high anharmonicity of

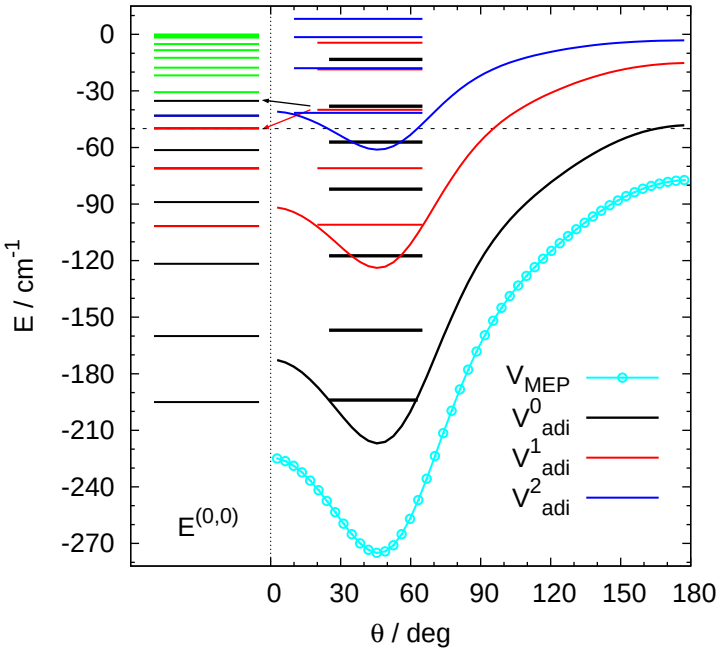


Figure 7. Minimum energy path $V_{\mathrm{MEP}}$ and effective angular profiles $V_{\mathrm{adi}}^{v_s}$ computed for the stretching states $v_s = 0 - 2$. The full-dimensional vibrational energies $E^{(0,0)}$ are shown on the left-hand side. The energy level stack on the right-hand side represents energies obtained in the adiabatic bend approximation. The circles along the MEP denote the discrete angular points used in the DVR-DGB calculations. The horizontal dotted line at -49.9 $\mathrm{cm}^{-1}$ shows the energy of the first vibrational state exhibiting pronounced vibrational mixing. The quantum labels $(v_b, v_s)$ for the first ten vibrational $E^{(0,0)}$ states are $(0,0)$, $(1,0)$, $(2,0)$ $(0,1)$, $(3,0)$, $(1,1)$, $(4,0)$, $(2,1)$ $(0,2)$, and $(5,0)$,

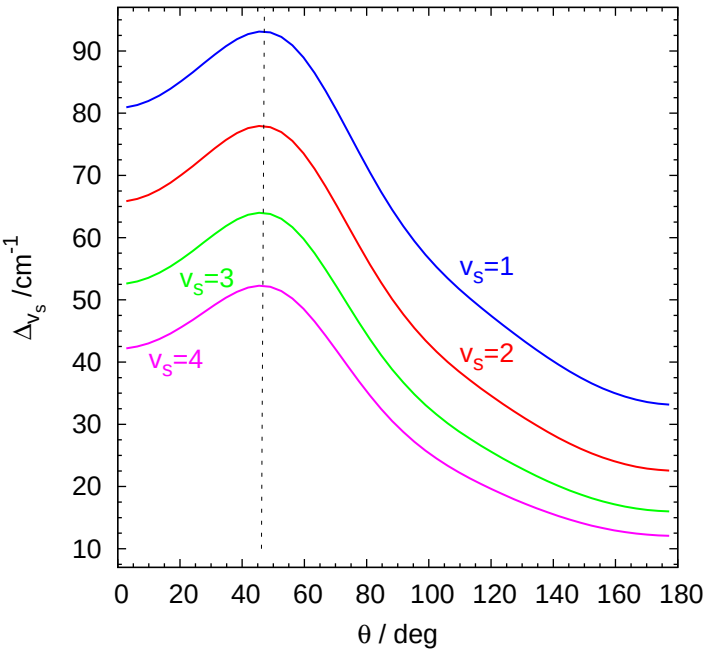


Figure 8. Variation of the effective one-dimensional vibrational spacing $\Delta_{v_s}$ in the stretching state $v_s$ with the Jacobi angle $\theta$, computed according to Eq. (17). The vertical dotted line shows the Jacobi angle $\theta_e$ at equilibrium.

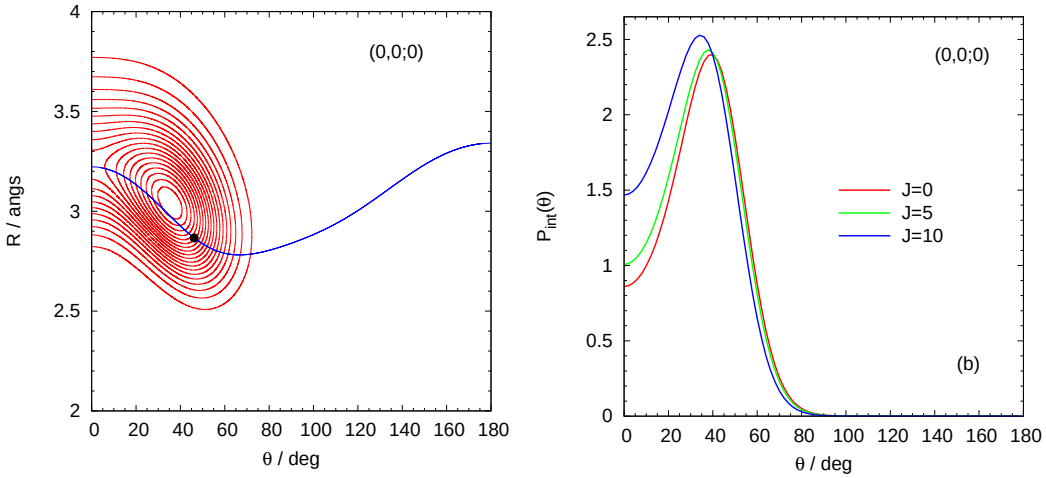


Figure 9. (a) Contour map of the wavefunction probability amplitude integrated over the Euler angles for the vibrational ground state $(0,0;0)$. Contours are drawn at intervals of 5% of the maximum wavefunction probability amplitude. The variation of the Jacobi distance along the angular minimum energy path is additionally shown. The solid circle shows the equilibrium geometry. (b) The wavefunction probability amplitude $P_{int}(\theta)$ integrated over the Euler angles and the radial coordinate $R$ for the vibrational ground state $(0,0;0)$ and $J = 0, 5$ and 10.

$\nu_s$.

The first seven vibrational levels lying below the ground-state adiabatic linearization barrier at $\theta = 180°$ are only exposed to a weak nonadiabatic coupling, as seen by small differences between the full-dimensional vibrational energies $E^{(0,0)}$ and their adiabatic counterpart in Figure 7. For these states, the quantum number assignments were easy to make by locating the dominant zero-order contribution in the corresponding adiabatic expansions. For levels above -50 $\mathrm{cm}^{-1}$, the nonadiabatic effects due to the kinetic coupling beyond the stretch-bend separation become prominent, leading to strong zero-order state mixing. The dominant vibrational mixing is found to be of Fermi type between $(v_b, v_s)$ and $(v_b - 2, v_s + 1)$.

A two-dimensional plot of the wavefunction probability amplitude for the ground vibrational state is depicted in Figure 9(a). The wavefunction is localized in the angular region $\theta \in (0°, 90°)$ and has a single maximum, close to the position of the minimum of the potential, but shifted to somewhat larger $R$ and smaller $\theta$, as seen from the vibrationally averaged geometry $\langle R \rangle = 3.05$ A and $\langle \theta \rangle = 42.7°$. A striking feature in Figure 9(a) is a large wavefunction amplitude at $\theta = 0°$. Further inspection of the other states showed that all vibrational wavefunctions explore the linearity region $\theta = 0°$. The first vibrational level fully delocalized in $\theta$ is the state $n^{0,0} = 6$, assigned as $(4,0;0)$, which lies about 10 $\mathrm{cm}^{-1}$ below the second adiabatic linearization barrier at -50 $\mathrm{cm}^{-1}$ in Figure 7. Vibrational levels lying above this energy are all extensively delocalized in the $\theta$ space and subject to pronounced angular-radial mixing. The onset of free-rotor structure in the bending progression also takes place at this energy. This effect has very important consequences for the overall rotation-vibration dynamics of the complex.

In weakly bound states, the vibrationally averaged Jacobi distance $\langle R \rangle$ for excited states can be rather large. We found, for instance, $\langle R \rangle$ of 6.1, 7.8, and 17.9 A for the levels $n^{(0,0)} = 16$, 17, and 18 lying at -1.72, -0.74, and -0.05 $\mathrm{cm}^{-1}$, respectively. We may, however, note that several positive energy states are identified, possessing $\langle R \rangle$ smaller than the largest bound state vibrationally averaged distance of 17.9 A, such as *e.g.* $\langle R \rangle$ of 5.2 and 7.6 A calculated for the levels at 1.8 and 2.9 $\mathrm{cm}^{-1}$, respectively. These states are expected to be metastable.

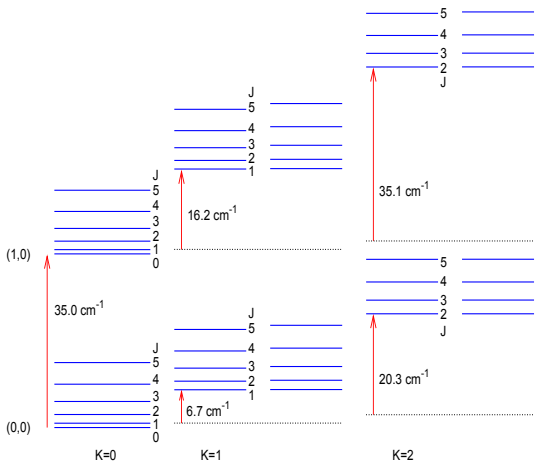


Figure 10. Rotational excitation of the ground $(0,0)$ and first bending $(1,0)$ vibrational state for $J = 0-5$, where the state label is $(v_b,v_s)$.

### 6.2. *Rotational structure*

Rotational excitation in the vibrational ground state and in the first bending state is schematically depicted for $J = 0-5$ and $K = 0-2$ in Figure 10. The quantum label $J$ describes the rotation of the complex as a whole ("end-over-end rotation") and $K$ the rotation about the body-fixed $z$ axis. In Figure 10, the $K = 1$ levels display pronounced $l$-type splitting, which amounts to 0.06 $cm^{-1}$ for $v_b = 0$ and to 0.08 $cm^{-1}$ for $v_b = 1$. The even-parity and odd-parity states for $K = 2$ and 3 differ by about $2{\cdot}10^{-4}$ and $3{\cdot}10^{-5}$ $cm^{-1}$ for $v_b = 0$ and by 0.0095 and 0.014 $cm^{-1}$ for $v_b = 1$.

The effective rotational constant $\overline{B}_v = (B_v + C_v)/2$ for the vibrational state $v$ was determined by a least squares fit to the following approximate expression

$$E_{vJ} = T_v + \overline{B}_v J(J+1) - D_v J^2(J+1)^2, \tag{18}$$

where $T_v$ stands for the vibrational term energy. The latter formula was used to fit the $K = 0$ levels of Figure 10. For the levels $(0,0;0)$ and $(1,0;0)$, we readily found effective rotational constants $\overline{B}_v$ of 0.4387 and 0.4285 $cm^{-1}$ and quartic centrifugal distorsion constants $D_v$ of $9{\times}10^{-5}$ $cm^{-1}$ and $4{\times}10^{-5}$ $cm^{-1}$, respectively. Furthermore, the $\overline{B}_v$ value for $v_b = 0$ nicely agrees with the result $(B_0+C_0)/2$ from Table 4, calculated from the $J = 0,1$ transitions only.

In view of Figure 10, it is clear that $K$ excitations do not follow the $K^2$ rule, expected in the limit of the (rigid) symmetric top. To satisfactorily fit the $K$-dependence of the rotational constant $A$ of He-$CO^+$, unreasonably high $K^2$ contributions were needed in the usual polynomial expansions in terms of $J(J+1)$ and $K^2$ [even with 9 polynomial terms involving pure $K^2$ parts the standard deviation of the fit was 0.02 $cm^{-1}$]. In other words, although the He-$CO^+$ complex possesses a nonlinear equilibrium structure, it was not possible to fit the rotational excitations to the reduced Hamiltonian for an asymmetric top even in the ground vibrational state. This contrasts with previous successful applications of the reduced Hamiltonian to fit rotational transitions in other nonlinear van der Waals complexes [65].

For triatomic molecules described by three Jacobi coordinates $r, R, \theta$ of Figure 1,

the principal moments of inertia are derived to be

$$\begin{aligned} I_1 &= \frac{1}{2}\left[I_r + I_R + \sqrt{I_r^2 + I_R^2 + 2I_rI_R\cos 2\theta}\right] \\ I_2 &= \frac{1}{2}\left[I_r + I_R - \sqrt{I_r^2 + I_R^2 + 2I_rI_R\cos 2\theta}\right] \\ I &= I_1 + I_2 \end{aligned} \tag{19}$$

where

$$\begin{aligned} I_r &= \mu_r r^2 = m_C m_O r^2/m_{CO} \\ I_R &= \mu_R R^2 = m_{\mathrm{He}} m_{\mathrm{CO}} R^2/m_{\mathrm{HeCO}} \end{aligned} \tag{20}$$

for He-$CO^+$. The rotational constant $A$ expressed as a wavenumber is, thus,

$$A = \frac{\hbar^2}{2hcI_2}. \tag{21}$$

For the T-shaped complex ($\theta = 90°$), $A$ is equal to the rotational constant $B(CO^+)$ since $I_r < I_R$. This can be easily seen from Eq. (19). Note that $\hbar^2/2hcI_R$ is about 0.4-0.6 $\mathrm{cm}^{-1}$ along the minimum energy path.

The rotational constant $A$ of Eq. (21) grows rapidly to infinity upon straightening of the angle $\theta$. Consequently, the effective vibrationally averaged rotational constant $A_v$ can be much larger than the equilibrium $A_e$ for vibrational states $v$, which have wavefunctions with considerable amplitudes at close-to-linearity arrangements [69]. This is exactly what we observe in Tables 4 and 7, giving $A_e = 4.4\,\mathrm{cm}^{-1}$ and $A_0 = 7.2\,\mathrm{cm}^{-1}$ in agreement with the wavefunction contour map of Figure 9(a).

We additionally computed the expectation values of the rotational constants, making explicit use of Eq. (19). Our results indicate high sensitivity of $\langle A\rangle$ on both $J$ and $K$. For the levels $(v_b, v_s; K)$ assigned as $(0,0;0)$, $(1,0;0)$, and $(0,1;0)$, for instance, we obtained $\langle A\rangle$ of 11.9, 42.4, and 20.0 $\mathrm{cm}^{-1}$ for $J = 0$ and of 13.0, 44.1, and 20.4 $\mathrm{cm}^{-1}$ for $J = 5$. This increase of $\langle A\rangle$ with increasing $J$ is in agreement with Figure 9(b), which shows the wavefunction probability amplitude $P_{int}(\theta)$ integrated over the Euler angles and the radial coordinate $R$ for the vibrational ground state and $J = 0, 5$ and 10. There, we see an increase of $P_{int}(\theta)$ at $\theta = 0°$ and significant shifts of the maximum of $P_{int}(\theta)$ towards smaller $\theta$ with increasing $J$.

The $K$ excitation leads to smaller $\langle A\rangle$ values. For the $K = 1$ states $(0,0;1)$, $(1,0;1)$, and $(0,1;1)$ for $J = 1$, we found $\langle A\rangle$ of 5.76, 9.24, and 7.56 $\mathrm{cm}^{-1}$, which are thus $2-4$ times smaller than the corresponding $K = 0$ results. The lowering of $\langle A\rangle$ with $K$ excitation can be understood with the help of Figure 11, showing the contour maps for the vibrational ground state and $K = 1, 3$ and 6. The maximum of the wavefunction probability amplitude for $K = 1$ in Figure 11(a) is close to the position of the potential energy minimum. The maxima for $K = 3$ and $K = 6$ are, however, shifted to larger $\theta$. The values of $\langle\theta\rangle$, computed as $\arccos(\sqrt{\langle\cos^2\theta\rangle})$, are found to be 46.1, 53.9, and 64.1° for $K = 1, 3$, and 6, respectively. The wavefunctions for the states of $K \neq 0$ are pushed away from the linearity regions at $\theta = 0, 180°$ by the centrifugal contribution, proportional to $f(r,R)/2\sin^2\theta$ for triatomic molecules, where $f(r,R) = (1/I_r + 1/I_R)$ is the inverse of the reduced mass associated with the bending vibration [70]. For the vibrational ground state, the expectation value $\langle f(r,R)\rangle$ shows a moderate variation with $K$, as seen from $\langle\hbar^2 f(r,R)/2hc\rangle$=2.495 $\mathrm{cm}^{-1}$ found for $K = 0$ and $\langle\hbar^2 f(r,R)/2hc\rangle$=2.532 $\mathrm{cm}^{-1}$ found for $K = 6$ (an

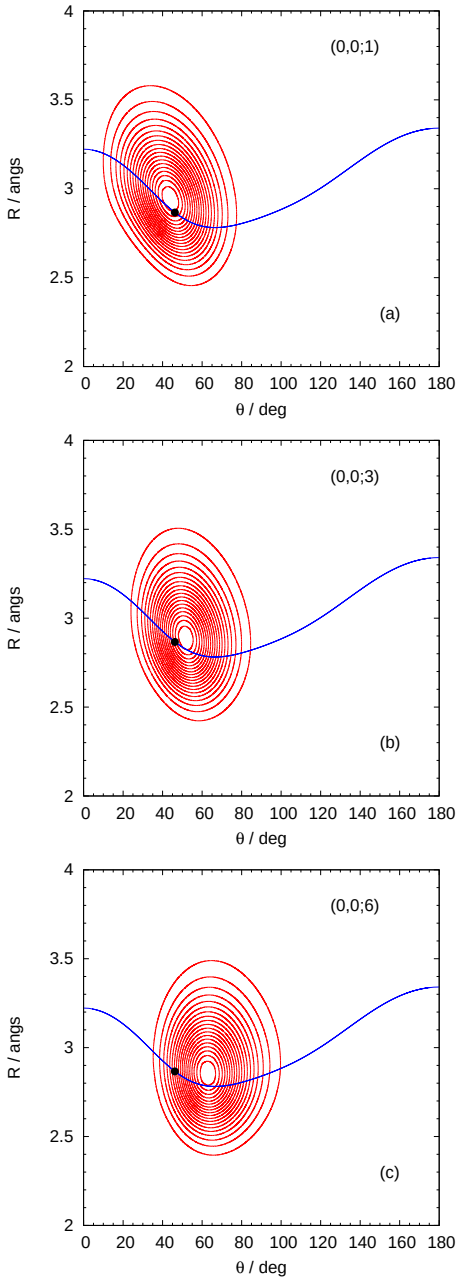


Figure 11. Contour maps of the wavefunction probability amplitude integrated over the Euler angles for the vibrational ground state and (a) $K = 1$, (b) $K = 3$, and (c) $K = 6$ obtained from $J = K$ calculations. Contours are drawn at intervals of 5% of the maximum wavefunction probability amplitude. The solid (blue online) curve shows the minimum energy path along the Jacobi angle. The solid circle indicates the equilibrium geometry.

increase of 1.5 %). On the other hand, the quantity $\langle \hbar^2 f(r,R)/2hc \sin^2\theta \rangle$ assumes values of 1.97, 1.03, 0.73, and 0.56 cm$^{-1}$ for respectively $K = 0, 1, 3$ and 6. In Figure 11(c), we may also note that the lack of "tilt" of the elliptical wavefunction contours for $K = 6$ compared to those for $K = 0$ and $K = 3$ indicates almost no angular-radial mixing for $K = 6$.

The $K$ dependence of the rotational constant $A$ was also analysed with the help of the effective rotational constant $A_K$, computed for a chosen $K$ and a given $J$ either as

$$A_{K,0} = \left[E_{(0,0;K)} - E_{(0,0;0)}\right]/K^2 \tag{22}$$

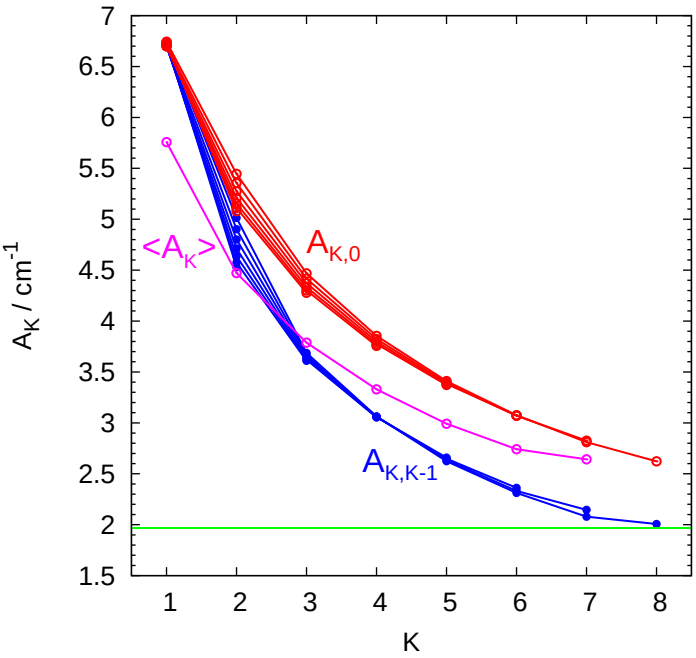


Figure 12. Effective rotational constants $A_{K,0}$ and $A_{K,K-1}$ computed for the ground vibrational state by means of Eqs. (22) and (23). The respective expectation values $\langle A_K \rangle$ are obtained with the help of Eq. (21). The horizontal line shows the rotational constant of the free $CO^+(^2\Sigma^+)$ monomer.

or as

$$A_{K,K-1} = \left[E_{(0,0;K)} - E_{(0,0;K-1)}\right] / (2K+1). \tag{23}$$

The latter quantities assume a constant value for a rigid rotor. The quantities $A_{K,0}$ and $A_{K,K-1}$ shown in Figure 12 are derived for the ground vibrational state from the even-parity rotational energies obtained for $J = 0 - 9$. The explicit values of the corresponding transition energies are collected in Table 8. Figure 12 also provides expectation values $\langle A_K \rangle$, computed by directly evaluating the vibrationally averaged $A$ given by Eq. (21). $A_K$ clearly exhibits a very pronounced variation with $K$. The difference between $A_{K,0}$ and $A_{K,K-1}$ increases with $K$ and is equal to 0.6 $cm^{-1}$ for $K = 8$. Note that the curve $A_{K,K-1}$ approaches the equilibrium rotational constant of the free $CO^+$ monomer from above for higher $K$. A rapid decrease of $A_K$ with increasing $K$ was previously observed for the HF dimer [71, 72] and explained by the quasilinearity of this complex [71, 73].

## 7. Conclusions

Our accurate potential surfaces combined with an advanced technique for the calculation of rotation-vibration states of floppy molecules have shown that the He-$CO^+$ ionic complex is a very interesting quasi-linear molecule which merits an up to date experimental study. The accurate energy levels should easily allow future spectroscopic checks of the quality of our potential energy surfaces which will be an important element to assess the accuracy of many-body models for $He_n$-$CO^+$ clusters and their use to compute effective rotational constants.

The adiabatic (frozen $r$) ground state energies for helium atoms interacting with $CO^+$ in its ground and first excited vibrational states decrease by about 0.4 $cm^{-1}$ (Table 7). This result is in perfect agreement with our diffusion quantum Monte Carlo (DMC) calculations. This change implies a small blue shift for $CO^+$ upon

Table 8. $K$ excitation in the ground vibrational state. Transition energies are given in $cm^{-1}$ relative to the respective ground state energy.

| $K/J$ | 1 | 2 | 3 | 4 | 5 | 6 | 7 | 8 |
|---|---|---|---|---|---|---|---|---|
| 1 | 6.74 | 6.73 | 6.72 | 6.71 | 6.70 | 6.70 | 6.71 | 6.74 |
| 2 | | 20.32 | 20.44 | 20.62 | 20.84 | 21.10 | 21.42 | 21.78 |
| 3 | | | 38.49 | 38.72 | 39.00 | 39.34 | 39.75 | 40.22 |
| 4 | | | | 60.10 | 60.39 | 60.75 | 61.17 | 61.66 |
| 5 | | | | | 84.32 | 84.58 | 84.90 | 85.28 |
| 6 | | | | | | 110.57 | 110.55 | 110.71 |
| 7 | | | | | | | 138.43 | 137.73 |
| 8 | | | | | | | | 167.83 |

complexation. Our DMC results for larger clusters indicate a non-monotonic evolution of this vibrational frequency shift reaching a maximum at about 10 helium atoms [29]. This result could be very easily checked in a cluster size selected high resolution experiment.

## Acknowledgements

This work has benefited from generous financial support from Agence Nationale de Recherche through the grant DYNHELIUM (ANR-08-BLAN-0146-01).

## References

[1] N.R. Erickson, R.L. Snell, R.B. Loren, L. Mundy and R.L. Plambeck, Astrophys. J. **245**, L83 (1981).
[2] W.B. Latter, C.K. Walker and P.R. Maloney, Astrophys. J. **419**, L97 (1993).
[3] A. Fowler, Mon. Not. R. Astron. Soc **70**, 176 (1909).
[4] A. Fowler, Mon. Not. R. Astron. Soc **70**, 484 (1910).
[5] T.A. Dixon and R.C. Woods, Phys. Rev. Lett. **34**, 61 (1975).
[6] W. Lindinger and D.L. Albritton, J. Chem. Phys. **62**, 3517 (1975).
[7] C.P. Lauenstein, M.J. Bastian, V.M. Bierbaum, S.M. Penn and S.R. Leone, J. Chem. Phys. **94**, 7810 (1991).
[8] J. Sanderson, H. Tanuma, N. Kobayashi and Y. Kaneko, J. Phys. B: At. Mol. Opt. Phys. **26**, L465 (1993).
[9] E.J. Bieske, A.M. Soliva, M.A. Welker and J.P. Maier, J. Chem. Phys. **93**, 4477 (1990).
[10] E.J. Bieske, A.M. Soliva, A. Friedmann and J.P. Maier, J. Chem. Phys. **96**, 28 (1992).
[11] E.J. Bieske, A.M. Soliva, A. Friedmann and J.P. Maier, J. Chem. Phys. **96**, 4035 (1992).
[12] E.J. Bieske, S. Nizkorodov, A. Friedmann and J.P. Maier, Int. J. Mass. Spec. Ion. Proc. **135**, 19 (1994).
[13] H. Verbraak, J.N.P. van Stralen, J. Bouwman, J.S. de Klerk, D. Verdes, H. Linnartz and F.M. Bickelhaupt, J. Chem. Phys. **123**, 144305 (2005).
[14] S. Grebenev, J.P. Toennies and A.F. Vilesov, Science **279**, 2083 (1998).
[15] F.A. Gianturco, M. Lewerenz, F. Paesani and J.P. Toennies, Chemistry Eur. J. **5**, 405 (1999).
[16] F.A. Gianturco, M. Lewerenz, F. Paesani and J.P. Toennies, J. Chem. Phys. **112**, 2239 (2000).
[17] K. von Haeften, S. Rudolph, I. Simanovski, M. Havenith, R.E. Zillich and K.B. Whaley, Phys. Rev. B **73**, 054502 (2006).
[18] J.A. Ramilowski and D. Farrelly, Phys. Chem. Chem. Phys. **14**, 8123 (2012).
[19] J. Tang and A.R.W. McKellar, J. Chem. Phys. **119**, 754 (2003).
[20] A.R.W. McKellar, J. Chem. Phys. **121**, 6868 (2004).
[21] A.R.W. McKellar, J. Chem. Phys. **125**, 164328 (2006).
[22] L.A. Surin, A.V. Potapov, B.S. Dumesh, S. Schlemmer, Y. Xu, P.L. Raston and W. Jäger, Phys. Rev. Lett. **101**, 233401 (2008).
[23] P.L. Raston, Y. Xu, W. Jäger, A.V. Potapov, L.A. Surin, B.S. Dumesh and S. Schlemmer, Phys. Chem. Chem. Phys. **12**, 8260 (2010).
[24] B. Shepperson, J. Lin, A.M. Ellis and S. Yang, J. Phys. Chem. A **115**, 7010 (2011).
[25] P.A. Hamilton, A.N. Hughes and K.D. Sales, J. Chem. Phys. **99**, 436 (1993).
[26] R.G.A.R. Maclagan, L.A. Viehland and A.S. Dickinson, J. Phys. B: At. Mol. Opt. Phys. **32**, 4947 (1999).

[27] V.F. Lotrich and A. van der Avoird, J. Chem. Phys. **118**, 1110 (2003).
[28] M.C. Salazar, I. Lugo, A.J. Hernandez and C. Manzanares, Theo. Chim. Acta **115**, 246 (2006).
[29] M. Mladenović and M. Lewerenz p. to be published (2013).
[30] C. Hampel, K.A. Peterson and H.J. Werner, Chem. Phys. Lett. **190** (1-2), 1 (1992).
[31] M.J. Deegan and P.J. Knowles, Chem. Phys. Lett. **227** (3), 321 (1994).
[32] H.J. Werner, P.J. Knowles, G. Knizia, F.R. Manby, M. Schütz, P. Celani, T. Korona, R. Lindh, A. Mitrushenkov, G. Rauhut, K.R. Shamasundar, T.B. Adler, R.D. Amos, A. Bernhardsson, A. Berning, D.L. Cooper, M.J.O. Deegan, A.J. Dobbyn, F. Eckert, E. Goll, C. Hampel, A. Hesselmann, G. Hetzer, T. Hrenar, G. Jansen, C. Köppl, Y. Liu, A.W. Lloyd, R.A. Mata, A.J. May, S.J. McNicholas, W. Meyer, M.E. Mura, A. Nicklass, D.P. O'Neill, P. Palmieri, D. Peng, K. Pflüger, R. Pitzer, M. Reiher, T. Shiozaki, H. Stoll, A.J. Stone, R. Tarroni, T. Thorsteinsson and M. Wang, MOLPRO, version 2012.1, a package of ab initio programs Cardiff, UK, 2012, see http://www.molpro.net.
[33] T.H. Dunning, Jr., J. Chem. Phys. **90**, 1007 (1989).
[34] R.A. Kendall, T.H. Dunning and R.J. Harrison, J. Chem. Phys. **96**, 6796 (1992).
[35] S.F. Boys and F. Bernardi, Mol. Phys. **19**, 553 (1970).
[36] T. Helgaker, W. Klopper, H. Koch and J. Noga, J. Chem. Phys. **106**, 9639 (1997).
[37] H.J. Werner and P.J. Knowles, J. Chem. Phys. **89**, 5803 (1988).
[38] P.J. Knowles and H.J. Werner, Chem. Phys. Lett. **145**, 514 (1988).
[39] H.J. Werner, Mol. Phys. **89**, 645 (1996).
[40] K.P. Huber and G. Herzberg, *Molecular Spectra & Molecular Structure Vol. IV. Constants of Diatomic Molecules* (Prentice-Hall, Englewood Cliffs, NJ, 1979).
[41] J.A. Coxon and S.C. Foster, J. Mol. Spectrosc. **93**, 117 (1982).
[42] D.H. Katayama and J.A. Welsh, J. Chem. Phys. **75**, 4224 (1981).
[43] D.H. Katayama and J.A. Welsh, J. Chem. Phys. **76**, 3848 (1982).
[44] U. Kleinekathöfer, M. Lewerenz and M. Mladenović, Phys. Rev. Lett. **83**, 4717 (1999).
[45] C.L. Pekeris, Phys. Rev. **45** (2), 98 (1934).
[46] K.K. Irikura, J. Phys. Chem. Ref. Data **36**, 389 (2007).
[47] R. Kępa, A. Kocan, M. Ostrowska-Kopeć, I. Piotrowska-Domagała and M. Zachwieja, J. Mol. Spectrosc. **228**, 66 (2004).
[48] R. Kępa, A. Kocan, M. Ostrowska-Kopeć, I. Piotrowska-Domagała and M. Zachwieja, J. Mol. Spectrosc. **230**, 102 (2005).
[49] P.B. Davies and W.J. Rothwell, J. Chem. Phys. **83**, 5450 (1985).
[50] P.J. Bruna and F. Grein, J. Chem. Phys. **127**, 2074107 (2007).
[51] J.K. Thompson, S. Rainville and D.E. Pritchard, Nature **430**, 58 (2004).
[52] J.F. Harrison, J. Phys. Chem. A **110** (37), 10848 (2006).
[53] J.Thomson and F.W. Dalby, Can. J. Phys. **46**, 2815 (1968).
[54] J.S. Muenter, J. Mol. Spectrosc. **55**, 490 (1975).
[55] P.A. Martin and M. Fehér, Chem. Phys. Lett. **232** (5£6), 491 (1995).
[56] T. Ebata, N. Hosoi and M. Ito, J. Chem. Phys. **65**, 3920 (1992).
[57] K. Pachucki and J. Sapirstein, Phys. Rev. A **63** (1), 012504 (2000).
[58] A.J. Thakkar, J. Chem. Phys. **75**, 4496 (1981).
[59] T.N. Olney, N.M. Cann, G. Cooper and C.E. Brion, Chem. Phys. **223**, 59 (1997).
[60] S. Kar and Y.K. Ho, Phys. Rev. A **80** (6), 062511 (2009).
[61] T.G.A. Heijmen, R. Moszynski, P.E.S. Wormer and A. van der Avoird, J. Chem. Phys. **107**, 9921 (1997).
[62] R.N. Zare, *Angular Momentum* (J. Wiley & Sons, New York, 1988).
[63] K. Yamada and M. Winnewisser, Z. Naturforsch. A **31**, 139 (1976).
[64] A.D. Buckingham, Adv. Chem. Phys. **12**, 107 (1967).
[65] O. Dopfer, R.V. Olkhov, M. Mladenović and P. Botschwina, J. Chem. Phys. **121**, 1744 (2004).
[66] W.H. Press, B.P. Flannery, S.A. Teukolsky and W.T. Vetterling, *Numerical Recipes* (Cambridge University Press, Cambridge, 1986).
[67] M. Mladenović and Z. Bačić, J. Chem. Phys. **94**, 4988 (1991).
[68] M. Mladenović, Spectrochim. Acta, Part A **58** (4), 795 (2002).
[69] M. Mladenović, M. Elhiyani and M. Lewerenz, J. Chem. Phys. **130**, 154109 (2009).
[70] M. Mladenović, J. Chem. Phys. **112** (3), 1070 (2000).
[71] A.S. Pine, W.J. Lafferty and B.J. Howard, J. Chem. Phys. **81**, 2939 (1984).
[72] K. von Puttkamer and M. Quack, Chem. Phys. **139**, 31 (1989).
[73] X.T. Wu, E.F. Hayes and A.B. McCoy, J. Chem. Phys. **110**, 2365 (1999).